



Research Article

Suppression of discontinuous precipitation and strength improvement by Sc doping in Cu-6 wt%Ag alloys



Bailing An^{a,b,d}, Rongmei Niu^d, Yan Xin^d, William L. Starch^d, Zhaolong Xiang^{a,b,d}, Yifeng Su^e, Robert E. Goddard^d, Jun Lu^d, Theo M. Siegrist^{d,f}, Engang Wang^{a,c,*}, Ke Han^{d,**}

^a Key Laboratory of Electromagnetic Processing of Materials (Ministry of Education), Northeastern University, Shenyang 110819, China

^b School of Materials Science and Engineering, Northeastern University, Shenyang 110819, China

^c School of Metallurgy, Northeastern University, Shenyang 110819, China

^d National High Magnetic Field Laboratory, Florida State University, Tallahassee, FL 32310, USA

^e Oak Ridge National Laboratory, Oak Ridge, TN 37830, USA

^f FAMU-FSU College of Engineering, Tallahassee, FL 32310, USA

ARTICLE INFO

Article history:

Received 12 May 2022

Revised 19 June 2022

Accepted 21 June 2022

Available online 29 July 2022

Keywords:

Sc doping

Grain boundary segregation

Precipitation

Strength

Electrical conductivity

Plastic deformation

ABSTRACT

In low-Ag Cu matrix alloys, the presence of coarse discontinuous precipitates may limit strength. We demonstrated that discontinuous precipitation was suppressed, and continuous precipitation was enhanced by the doping of Cu-6 wt%Ag with Sc. A high-volume fraction of continuous precipitates, which nucleated on {111} planes, led to a 55 MPa increase in strength, with only a slight decrease in electrical conductivity. The addition of Sc inhibited the nucleation of discontinuous precipitates by causing the Sc and the Ag to co-segregate onto grain boundaries, thus forming a thin intermetallic compound layer between grains. After deformation, both discontinuous and continuous precipitates were drawn into Ag fibers. The combination of deformation strain and doping caused an increase in density and a decrease in the diameter of Ag fibers, resulting in about 205 MPa increase in doped samples when the deformation strain reached 4.9. The thinner, denser Ag fibers in the doped samples also caused higher electron scattering at interfaces, leading to electrical conductivity that was 11% IACS lower than in non-doped samples. For reference, 100% IACS (International Annealed Copper Standard) is equivalent to $1.7241 \mu\Omega \text{ cm}$.

© 2022 Published by Elsevier Ltd on behalf of The editorial office of Journal of Materials Science & Technology.

1. Introduction

Cu-Ag alloys doped with different alloying elements are known for high strength and high conductivity and are widely used as conductors in high field magnets, as combustion chamber liners of liquid rocket engines, and as conductors for electronic components [1–7]. The materials in high-field magnets, which are fabricated into wires or disks, reach exceptionally high strength. This results from a high density of Ag precipitates that lengthen into long fibers [8–11]. The resulting multiplicity of Cu/Ag interfaces prevents dislocation movement, thus increasing strength [12].

In Cu-Ag alloys, continuous precipitates (CPs) have smaller size and spacing than discontinuous precipitates (DPs), leading to a higher density of Ag fibers after deformation, thus are more ef-

fective in preventing dislocation movement [10,13]. When Ag content reaches 24 wt%, researchers observed that most of its Ag precipitates are CPs rather than DPs [14]. Some researchers have attempted to decrease the cost of conductors by decreasing Ag content, but in the Cu-Ag with lower Ag content, the Ag may take the form of DPs as well as CPs [13,15]. Because of the larger size and spacing of DPs, their presence in large numbers limits the strength of the alloys [16,17]. Cu-6 wt%Ag, for example, has no CPs at all, only DPs [9]. Its strength is around 13% lower than that of Cu-24 wt%Ag after they were cold rolled to a total reduction of 94% with the same method [18].

Discontinuous precipitation is a solid-state precipitation reaction distinguished by a migrating reaction front that provides a conduit for faster transport [19]. The regions on both sides of the reaction front have different crystallographic zone axes and significantly different solute concentrations. This feature does not appear in continuous precipitation [17,20]. It has been observed in many alloys and generally has a deleterious effect on strength, as well as other mechanical and physical properties [21]. Therefore, to suppress discontinuous precipitation, two methods have been found.

* Corresponding author at: School of Metallurgy, Northeastern University, Shenyang 110819, China.

** Corresponding author.

E-mail addresses: egwang@mail.neu.edu.cn (E. Wang), han@magnet.fsu.edu (K. Han).

The first approach is to avoid high-energy grain boundaries because they are usually the nucleation sites of DPs [22,23]. These boundaries (e.g., with the energy of about 0.5 J/m² [24]) usually have high angles, except for the ones with high coincident site lattices (e.g., with 0.016 J/m² for the twin boundaries of Cu-Ag solid solution [25]). The second is doping with a suitable third element [21,26,27]. An explanation, developed by Williams and Butler, stated that doping with a third element caused strong grain boundary segregation [28]. The distribution of solutes at the grain boundary suppresses discontinuous precipitation because they lead to (1) lower grain boundary energy [29], (2) lower grain boundary mobility [30], and (3) lower diffusion rate of solute atoms [31].

Because the energy of grain boundaries is very difficult to control in Cu-Ag, extensive research focused on doping with a third element. Fe, Cr, Nb, Zr, and certain rare-earth elements have been added to Cu-Ag alloys [32–36]. Of these elements, only Nb and Zr have been found to partially suppress discontinuous precipitation. Recently, we found that doping with Sc totally suppressed discontinuous precipitation in Cu-3 wt%Ag, leaving the electrical conductivity almost the same in doped and non-doped samples after deformation at a low level of strain [37]. There are two advantages of Sc for alloy casting. One is the melting point of Sc, which is approximately 300 °C lower than that of Zr and 928 °C lower than that of Nb [38–40]. The other one is the solubility of Sc in Ag, which is significantly larger than that of Zr and Nb in Ag (for Sc in Ag at 900 °C: 10.3 wt%, for Zr in Ag at 900 °C: 0.08 wt%, for Nb in Ag at 900 °C: extremely small), which is more beneficial for master alloy fabrication [41–44].

In this work, we investigated the microstructure and properties of Cu-6 wt%Ag (non-doped sample) and Cu-6 wt%Ag doping with 0.05 wt%Sc, 0.10 wt%Sc, and 0.15 wt%Sc (doped samples) before and after deformation, and would like to answer the following four questions: (1) In non-doped and doped samples, what fundamental difference exists between DPs and CPs; (2) By what mechanism does Sc suppress discontinuous precipitation. (3) What configuration of Ag fibers occurs in non-doped and doped samples; (4) By what mechanism does each configuration affect tensile strength and electrical conductivity.

2. Materials and methods

We made one non-doped and three doped ingots (the low Sc content was used to avoid the formation of large intermetallic compound particles [37]) (see Appendix A). The eutectic component that formed during solidification had a lower melting point than the original alloy—as low as 779 °C [16,45]. To avoid undesirable melting, we removed the eutectic at the start of heat treatment. We did this by subjecting the four ingots to solution treatment in two steps: (1) they were heated under an argon atmosphere to 760 °C, held for 4 h at that temperature, then quenched in water; (2) they were reheated in the same furnace to 790 °C, held for 6 h, then quenched in water. This temperature is sufficiently high to dissolve most Ag and Sc and is also the highest one without overheating our alloys. Afterwards, samples

were cut from each ingot and were aged at different temperatures. They were used for electrical resistance testing, hardness testing, and microstructure observation. The microstructure of as-cast and solution-treated samples is shown in Appendix B.

All four solution-treated ingots were aged at 450 °C for 8 h and air-cooled to room temperature. Afterwards, they were swaged into rods, which then were drawn into wires at room temperature. Deformation strain (ε) reached 4.9 ($\varepsilon = \ln(C_0/C)$, where C_0 and C are the initial and final cross-sectional area), and the average area reduction for each drawing was around 20%. There was no intermediate aging treatment during the whole deformation process. Samples were taken at different strains for electrical resistance testing, hardness testing, and microstructure observation.

Electrical resistance was tested in deionized water (22 °C) and liquid nitrogen (−196 °C), using a standard four-point probe method. Hardness was tested using a diamond indenter under a load of 0.3 kg for a dwelling time of 10 s. Tensile testing in displacement-controlled mode was carried out at room temperature using a Tytron 250 machine with an initial strain rate of $1 \times 10^{-4} \text{ s}^{-1}$. The strain was measured with a digital image correlation system (see Appendix C).

X-ray diffraction (XRD) was performed using a Scintag reflection diffractometer with Cu $K\alpha$ radiation diffracted beam analyzer. The XRD samples were prepared with Si powder (SRM 640e, provided by the National Institute of Standards & Technology), which was used as an internal standard for the proper analysis of the lattice parameters. We mixed the Si powder with ethanol and dropped the mixture onto the surface of each sample. After the ethanol evaporated, it left a thin film of Si powder. Each sample was subjected, first, to fast scanning from 30° to 100° in a step of 0.02° and subsequently to slow scanning in four ranges (from 41° to 45°, 46° to 52°, 55° to 58°, and 72° to 75°) in a very small step size of 0.0025°. All XRD curves were fitted according to the Pseudo-Voigt function with the MDI Jade 6 program. All Cu peaks were calibrated by Si peaks (see Appendix D). Lattice constants were calculated by Cohen's method, which can reduce the random errors and systematic errors produced on the Bragg angle tests [46]. Vegard's law was applied to subsequent analysis of the amount of Ag dissolved in Cu [47].

Differential scanning calorimetry (DSC) data were collected using a Shimadzu DSC-60. Solution-treated non-doped and doped samples were cut into 3.5 mm × 3.5 mm squares. Each square was ground down to a weight of around 20 mg, then sealed in an aluminum pan (ϕ 5 mm) and heated from room temperature to 550 °C in an argon atmosphere. Groups of samples were subjected to different constant heating rates: 5 °C/min, 10 °C/min, 20 °C/min, 30 °C/min, and 40 °C/min.

Using Energy Dispersive X-ray Spectrometer (EDS) in Zeiss 1540 XB field emission scanning electron microscopy (FESEM), we measured the content of Ag and Sc in each solution-treated ingot (Table 1). Ag precipitates were examined with FESEM after samples had been subjected to electropolishing in a solution of 30% H₃PO₄ and 70% deionized water with a voltage of 8 V and a cur-

Table 1
Ag and Sc content in each ingot after solution treatment*.

Sample	Ag		Sc	
	wt%	at%	wt%	at%
Cu-6 wt%Ag	5.83 ± 0.29	3.52 ± 0.18	0	0
Cu-6 wt%Ag-0.05 wt%Sc	5.67 ± 0.10	3.42 ± 0.06	0.03 ± 0.03	0.04 ± 0.05
Cu-6 wt%Ag-0.10 wt%Sc	5.61 ± 0.07	3.38 ± 0.04	0.11 ± 0.06	0.16 ± 0.09
Cu-6 wt%Ag-0.15 wt%Sc	5.85 ± 0.22	3.53 ± 0.13	0.13 ± 0.07	0.19 ± 0.10

* Ag content (the average value from at least five areas) was tested with EDS at low magnification in FESEM.

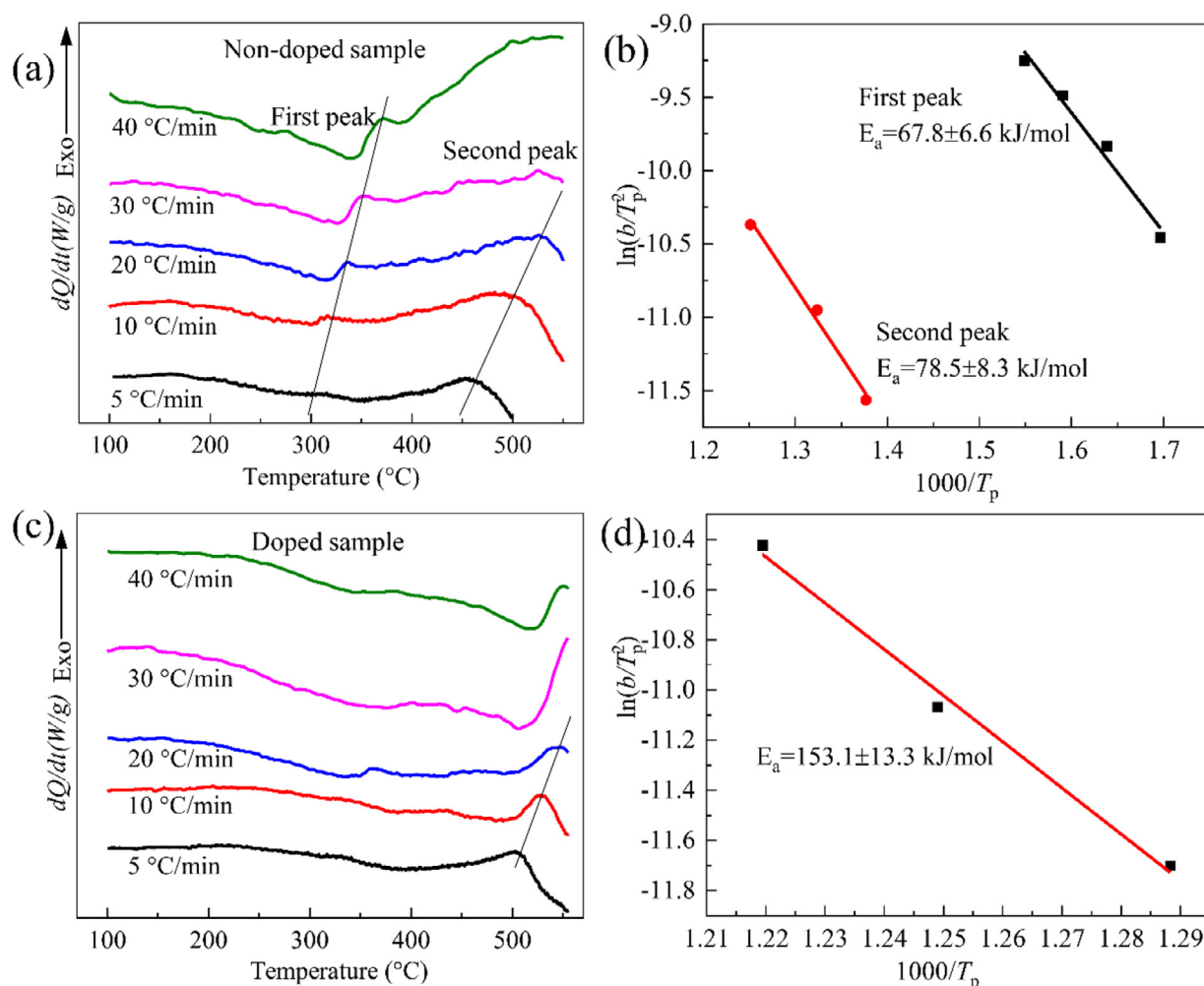


Fig. 1. DSC results of non-doped samples and doped samples (0.15 wt% Sc). (a, c) DSC curves of non-doped and doped samples, respectively, at different heating rates. (b, d) Plots for estimation of the activation energy of the peaks. The activation energy was calculated according to the slope of each line.

rent of 4 Å. Ag fibers were examined with FESEM after samples were etched in a solution of 30% HNO_4 and 70% deionized water. Using JEOL-2011 transmission electron microscope (TEM) and JEM-ARM200CF scanning transmission electron microscope (STEM), we examined the microstructure of samples before and after deformation. All TEM/STEM specimens were subjected to argon ion-milling at 5 kV at 7°.

3. Results

3.1. DSC results

DSC curves of exothermic reactions in non-doped samples showed two peaks, the first for discontinuous precipitation (between 300 and 400 °C) and the second for continuous precipitation (above 450 °C). Similar results were found in Cu-8 wt%Ag [13]. In samples doped with 0.15 wt% Sc, however, there was only one peak, above 500 °C, for continuous precipitation. As the heating rate increased, peaks in both doped and non-doped samples shifted toward higher temperatures (Fig. 1(a,c)). The following formula describes this shift for each peak [48]:

$$\ln\left(\frac{b}{T_p^2}\right) = -\frac{E_a}{RT_p} + C \quad (1)$$

where T_p represents the absolute temperature, b the heating rate, and E_a the activation energy. R is the universal gas constant and C is an arbitrary constant. For non-doped samples, the E_a of continuous precipitation was higher than that of discontinuous precipitation (Fig. 1(b)). Doping resulted in diminishing of the peak for discontinuous precipitation. The value of E_a of continuous precipitation (153 kJ/mol) in doped samples greatly exceeded that (68 kJ/mol) of non-doped samples (Fig. 1(b, d)).

3.2. XRD results

Non-doped and doped samples were both aged at 450 °C for 2 h and 16 h. They were then subjected to XRD testing. In all samples, as aging time increased, Cu peaks moved slightly to the right and a new $(111)_{\text{Ag}}$ peak appeared (Fig. 2(a–c)). Taking the movement of the Cu peaks into consideration, we calculated lattice constants of all samples and found that they all decreased after aging, but doped samples always had larger lattice constants than non-doped samples both before and after aging treatment. The lattice constant of non-doped samples decreased quickly within the first 2 h but very slowly after a longer aging time. The lattice constants of doped samples decreased more slowly than that of non-doped samples within the first 2 h but faster thereafter (Fig. 2(d)). The dissolved Ag in non-doped samples was then calculated by using the lattice constants (Table 2).

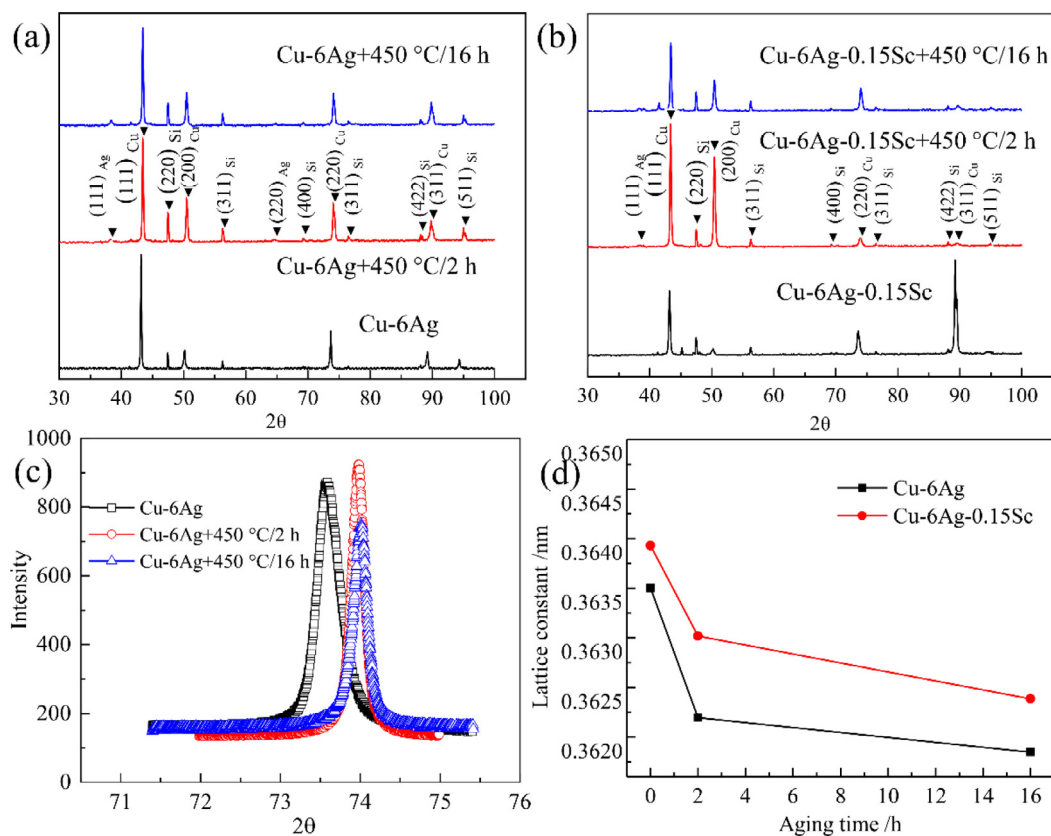


Fig. 2. XRD results of non-doped and doped samples after solution treatment and after aging at 450 °C for 2 h and 16 h. (a, b) XRD spectra (between 30° and 100°) for non-doped samples and doped samples (0.15 wt% Sc), respectively. (c) XRD spectra (between 71° and 75°) showing a shift of the $(220)_{\text{Cu}}$ peak of non-doped samples after aging treatment. (d) Change in lattice constants with respect to aging times.

Table 2

Lattice constants and corresponding amounts of dissolved Ag in non-doped and doped samples.

Sample	Lattice constant (nm)	Amount of Ag in Cu (at%)
Cu-6Ag	0.363372	3.97*
Cu-6Ag+450 °C/2 h	0.362194	1.47
Cu-6Ag+450 °C/16 h	0.361848	0.74
Cu-6Ag-0.15Sc	0.363501	N/A**
Cu-6Ag-0.15Sc+450 °C/2 h	0.363166	N/A**
Cu-6Ag-0.15Sc+450 °C/16 h	0.362343	N/A**

* The estimated dissolved Ag content in solution-treated non-doped samples is higher than the quantity added. This was also found in Piyawit's research [49].

** The dissolved Ag content in Cu-Ag-Sc cannot be calculated using Vegard's law due to two variables.

3.3. Microstructure and properties of samples after isochronal aging treatment

3.3.1. Microstructure of samples after aging for 2 h

When we compared non-doped with doped samples (0.15 wt% Sc), we found that the distribution and type of Ag precipitates varied after 2 h of aging treatment, depending on whether the samples were treated at 400 °C, 450 °C, or 500 °C. In non-doped samples, only DPs, which nucleated on grain boundaries, formed after aging treatment, regardless of aging temperature. After treatment at 400 °C, DPs were randomly distributed throughout the sample, but after treatment at 450 °C and 500 °C, the DPs begin to grow larger and coarser (Fig. 3(a–c)). After treatment of doped samples at 400 °C, we found no Ag precipitates at low magnification (SEM), but after treatment at 450 °C and 500 °C, we found both DPs and CPs, with CPs occupying most areas of the samples (Fig. 3(d–f)).

Under TEM, samples revealed very fine CPs arranged in lines inside grains (Fig. 4(a, b)). We also found that both Ag and Sc concentrated at grain boundaries in doped samples aged at 400 °C but none in solution-treated samples (Figs. 4(c, d) and 5). In some cases, thin intermetallic compound layers (Cu_3AgSc) had formed between adjacent grains (Fig. 4(c, d)).

The arrangement of CPs was different in different directions (Fig. 6). To clarify the distribution of precipitates, we focused on two Ag lines and tilted the sample approximately 56° from $[\bar{1}12]$ zone axis to $[\bar{1}10]$ zone axis. As we did this, the lines gradually broadened to stripes (Fig. 7). We then built a 3-D model to link the lines with the stripes, using the 2-D images taken by TEM in different orientations. We found that most CPs in doped samples lay on $\{111\}$ planes (Fig. 8). This was in contrast to the CPs in Cu-24wt%Ag, which lay on $\{001\}$ planes [14]. The CPs in doped samples nucleated at dislocation and stacking faults to reduce the in-

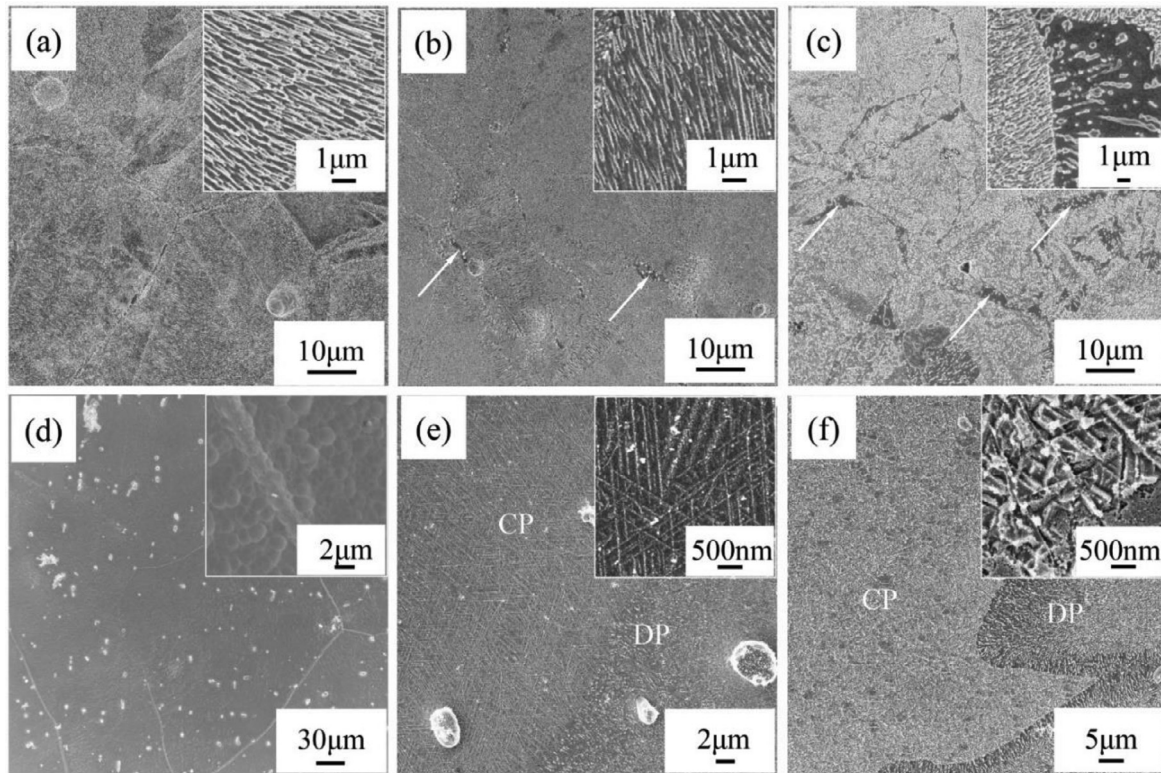


Fig. 3. SEM images of non-doped and doped samples aged for 2 h at 400 °C, 450 °C, and 500 °C, respectively. (a–c) Images showing DPs in non-doped samples. White arrows indicate discontinuous coarsening. Insets show high magnification images of the same DPs in (a), (b), and (c), respectively. The dark area in (c) shows the Cu matrix exposed between coarse DPs. (d–f) Images showing microstructure in doped samples. Insets show high magnification images of CPs in (d), (e), and (f), respectively. No Ag precipitates appear in (d).

interface energy in a unit area between Cu and Ag. The dislocations glided on {111} planes, and the stacking faults expanded on {111} planes, resulting in CPs distributed on the {111} planes [20]. Since the CPs in Cu-24wt%Ag have higher Ag content and thus higher driving force for the formation of CPs, it is unnecessary for CPs to keep on {111} planes [8,50–52]. We also found some Sc-rich precipitates in areas with CPs. The analysis is shown in Appendix E.

3.3.2. Properties of samples after aging for 2 h

We tested the electrical conductivity of both non-doped and doped samples that had been aged at various temperatures. After aging at 400 °C, the non-doped samples had an increase of 6.4% IACS in electrical conductivity while the doped samples remained unchanged. After aging at 450 °C, the non-doped samples reached a maximum electrical conductivity value of 92.5% IACS, while the conductivity of the doped samples did not reach its maximum until the aging temperature increased to 475 °C. The conductivity values of doped samples were around 85% IACS, slightly lower than the maximum reached by non-doped samples (Fig. 9(a)). The Residual Resistivity Ratio (RRR) was determined by comparing each sample's resistivity in deionized water and in liquid nitrogen. Our data showed that the doped samples had a lower RRR than the non-doped samples (Fig. 9(b)).

We tested hardness in both non-doped and doped samples. After aging at 400 °C, the hardness of the non-doped samples reached a maximum value of 92 HV, while the hardness of the doped samples was nearly unchanged. After aging at 450 °C, however, all the doped samples surpassed the non-doped samples. At this point, the samples with higher levels of doping, 0.10 wt% Sc and 0.15 wt% Sc, reached their maximum hardness of 129 HV and 133 HV, respectively (Fig. 9(c)).

Table 3

Tensile properties of non-doped and doped samples*.

Sample	$\sigma_{(0.2)}$ (MPa)	σ_U (MPa)	Elongation (%)
Cu-6Ag	143 ± 8	186 ± 9	13.3 ± 3.1%
Cu-6Ag + 450 °C/2 h	200 ± 14	259 ± 4	13.3 ± 2.3%
Cu-6Ag-0.15Sc	155 ± 4	201 ± 10	12.3 ± 2.5%
Cu-6Ag-0.15Sc + 450 °C /2 h	309 ± 20	314 ± 22	2.2 ± 0.7%

* $\sigma_{(0.2)}$: Strength at $\varepsilon = 0.002$, σ_U : Ultimate tensile strength.

After solution treatment, tensile testing was performed on non-doped samples and on doped samples (0.15 wt% Sc). At this point, because of the solution hardening of Sc, the doped, solution-treated samples had an ultimate tensile strength (UTS) that was 15 MPa higher than that of the non-doped samples. After aging at 450 °C for 2 h, the UTS increased for both doped and non-doped samples, but more in the doped samples, with average UTS now 55 MPa higher than that of the non-doped samples (Fig. 9(d), Table 3).

3.4. Microstructure and properties of samples after deformation

3.4.1. Microstructure of samples after deformation

All four ingots (Cu-6wt%Ag, Cu-6wt%Ag-0.05wt%Sc, Cu-6wt%Ag-0.10wt%Sc, and Cu-6wt%Ag-0.15wt%Sc) were aged at 450 °C for 8 h to increase electrical conductivity, and they were then drawn into wires. When ε was at 4.9, both CPs and DPs had taken the shape of fibers (Figs. 10(a) and 11(a)). In non-doped samples, the transverse cross-sectional images showed all Ag fibers that had evolved from DPs (FDPs) were distributed uniformly, with volume fraction (f_{Ag}) and diameter (d_{Ag}) of $4.7\% \pm 1.2\%$ and 3.2 ± 0.7 nm, respec-

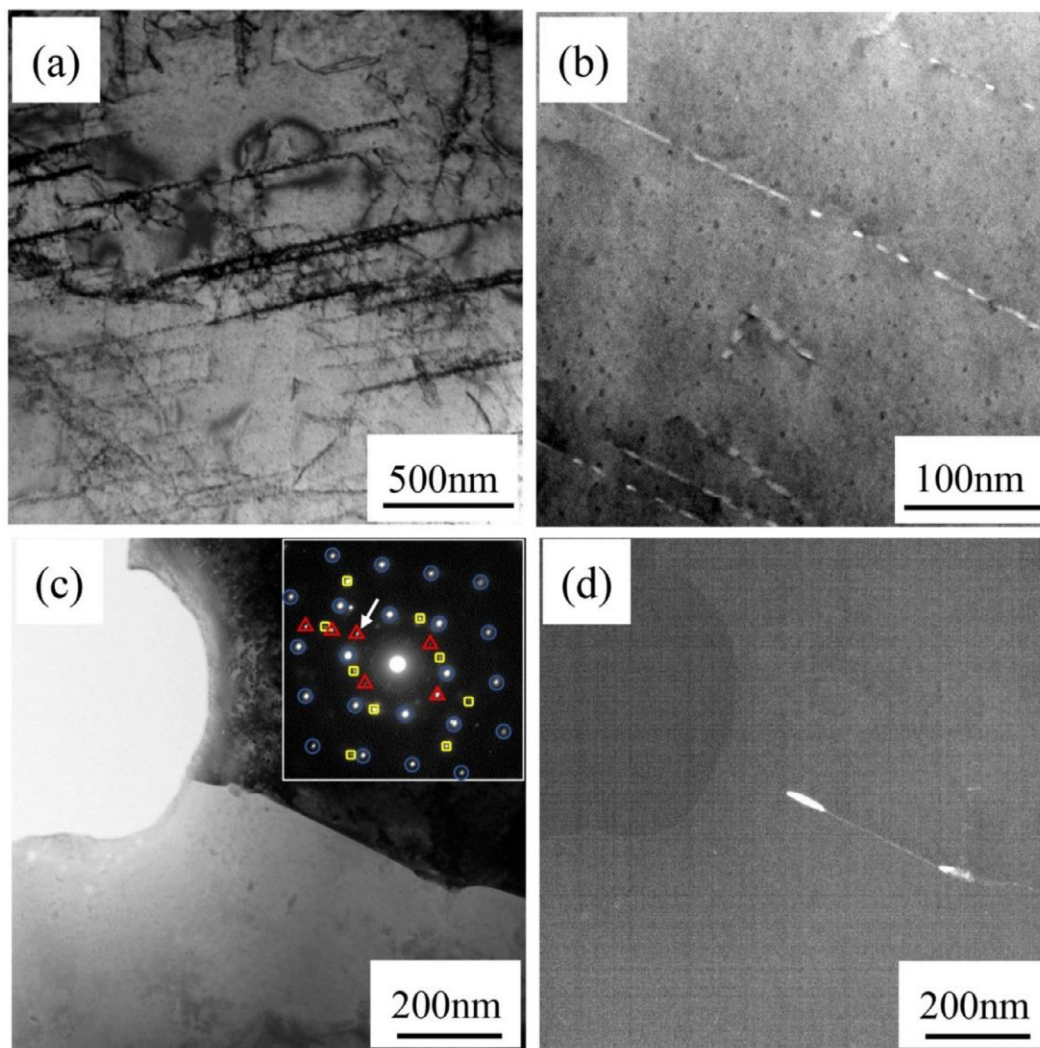


Fig. 4. TEM/STEM data for a doped sample (0.15 wt% Sc, aged at 400 °C for 2 h). (a) TEM bright field of CPs (in black lines). (b) High-angle annular dark-field scanning transmission electron microscopy (HAADF-STEM) image of CPs. (c) TEM bright-field image of the boundary between a dark and a light grain. The zone axis of the dark grain is [011], of the light grain, near $[1\bar{1}2]$. The inset shows the selected area diffraction pattern (SADP) of the two grains and the boundary, with circles marking the spots from the dark grain, squares marking the spots from the light grain, and triangles marking the spots from the intermetallic compound at the grain boundary. (d) TEM dark field image of the same grain boundary area, using the intermetallic spot marked by a small white arrow in the previous inset.

tively (Fig. 10(c)). In the doped samples (0.15 wt% Sc), SEM images showed Ag fibers only near grain boundaries (Fig. 11(b, c)). We assumed that these fibers had evolved from DPs because DPs in the doped samples were known to be arranged around grain boundaries (Fig. 3(e,f)). TEM images at higher magnification showed that the Ag fibers that had evolved from CPs (FCPs) were arranged in the doped samples as interleaved lines within the grains (Fig. 11(d, e)). Their f_{Ag} and d_{Ag} were $4.6\% \pm 0.9\%$ and 1.8 ± 0.2 nm. The mean random edge-to-edge distance (λ_f) of FDPs and FCPs was calculated with Fullman's equation [53]. They were 43.3 ± 2.1 nm and 25.9 ± 5.1 nm, respectively. Therefore, the λ_f of FCPs was less than that of FDPs.

In both types of samples, transverse cross-sectional images show misfit dislocations on Cu/Ag interfaces even though the diameter of fibers was only about 1.8 nm (Fig. 10(d, f)). Some longitudinal cross-sectional images of doped samples, however, did not show any misfit dislocations on Cu/Ag interfaces when the fiber diameter was about 2.5 nm (Fig. 13). Some deformation twins (as thin as 2 nm) appeared in the doped samples (Fig. 13(b, c)). In the non-doped samples, recrystallized Cu grains and coarsened Ag particles appeared in local areas, but none appeared in the doped

samples (Figs. 10(c) and 11(d)). Instead, there were many subgrains in the doped sample with numerous FCPs diffused along their boundaries (Fig. 12).

3.4.2. Properties of samples after deformation

We tested the electrical conductivity, RRR, and hardness of samples deformed to different strain values. As ε increased, electrical conductivity and RRR decreased in both doped and non-doped samples. When ε increased to 4.9, electrical conductivity in doped and non-doped samples decreased to around 66% IACS and 77% IACS, respectively, and the RRR decreased to around 2.5 and 3.2 (Fig. 14(a, b)). The hardness of both doped and non-doped samples increased as ε increased. At $\varepsilon = 4.9$, hardness values in doped and non-doped samples were around 290 HV and 249 HV, respectively. The hardening rate for doped samples was around 35 HV per unit of strain, higher than the rate for non-doped samples (31 HV per unit of strain).

We performed tensile testing on both non-doped and doped samples that had been deformed to a strain of 4.9 (Fig. 14(d)). All doped samples had UTS of around 1070 MPa, about 205 MPa higher than the average UTS of non-doped samples (Table 4). We

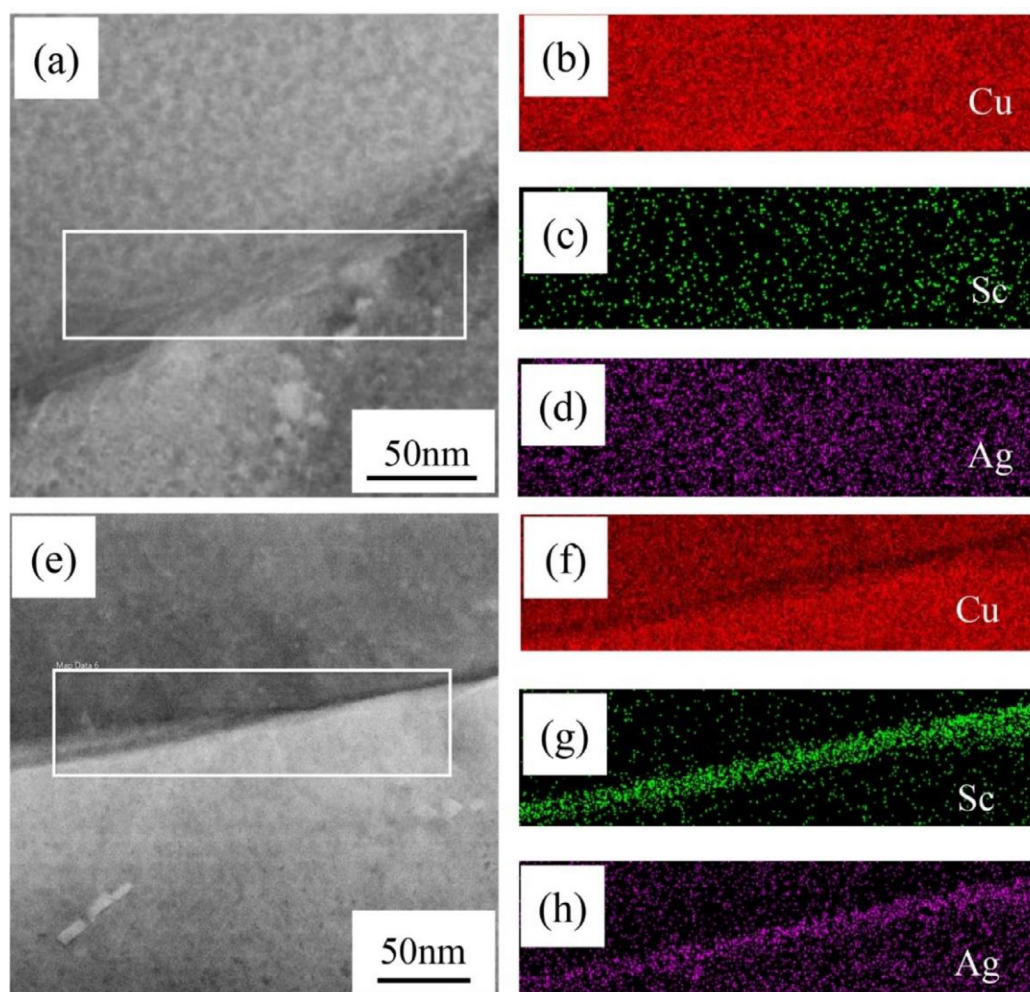


Fig. 5. HAADF-STEM images and EDS maps of grain boundaries in doped samples (0.15 wt% Sc). (a, e) Images of the grain boundaries in solution-treated sample and sample aged at 400 °C for 2 h. The rectangular outlines indicate the EDS-mapped areas. (b, c, and d) Element mapping images of Cu, Sc, and Ag, respectively, in (a). (f, g, and h) Element mapping images of Cu, Sc, and Ag, respectively, in (e). From the mapping, the atomic ratio among Cu : Ag : Sc is close to 60 : 20 : 20.

Table 4

Tensile properties and electrical conductivity of non-doped and doped samples at $\varepsilon = 4.9^*$.

Sample	$\sigma_{(0.2)}$ (MPa)	σ_U (MPa)	Conductivity (% IACS)
Cu-6Ag	844 ± 10	865 ± 19	77.2
Cu-6Ag-0.05Sc	1022	1065	67.9
Cu-6Ag-0.10Sc	1034 ± 3	1072 ± 3	64.6
Cu-6Ag-0.15Sc	1014 ± 69	1073 ± 45	66.2

* E: Young's modulus, $\sigma_{(0.2)}$: Yield Strength, σ_U : Ultimate tensile strength.

also tested the properties of deformed samples ($\varepsilon = 4.9$) aged at 300 °C for various time intervals (see Appendix F). The UTS of samples aged for 1 h was marginally lower than that of unaged samples, while conductivity was higher by about 6.3% IACS (Table F1).

4. Discussion

4.1. Differences between discontinuous and continuous precipitation

DPs began to form at lower aging temperatures and after shorter aging times than CPs. The main reason was the difference in their nucleation sites: DPs nucleated at grain boundaries, and CPs nucleated inside grains. After nucleation, growth occurred in

DPs as atoms migrated either through interfaces or grain boundaries, both of which provide conduits for faster transport of solute [21]. In other words, discontinuous precipitation was related to a higher diffusion rate of Ag than did continuous precipitation. This was reflected by lower activation energy (67.8 kJ/mol) for discontinuous precipitation and higher activation energy (79 kJ/mol) for continuous precipitation for non-doped samples. For doped samples, the CPs occurred at a higher temperature. We deduced that, at the same temperature, they would have formed at a lower rate than CPs in non-doped samples. This was also reflected by higher activation energy (153 KJ/mol) for CPs in doped than that (79 KJ/mol) in non-doped samples. The presence of Sc led to a smaller number of Ag atoms to overcome the activation energy barrier for CPs.

The different diffusion rate of Ag was confirmed by the lattice constants of undeformed non-doped and doped samples. Dissolved Ag in non-doped samples decreases sharply from 3.52 at% to 1.47 at% after aging for 2 h at 450 °C, but it decreases only slightly with additional aging time, from 1.47 at% to 0.74 at% (Table 2). In other words, most of the dissolved Ag in the non-doped samples must have precipitated from the Cu matrix in the first 2 h of aging. Dissolved Ag in the doped samples could not be calculated using Vegard's law because of the presence of Sc, but we were able to use lattice constants to estimate the amount of Ag plus Sc. Lattice constants decreased more slowly in doped than in non-doped samples

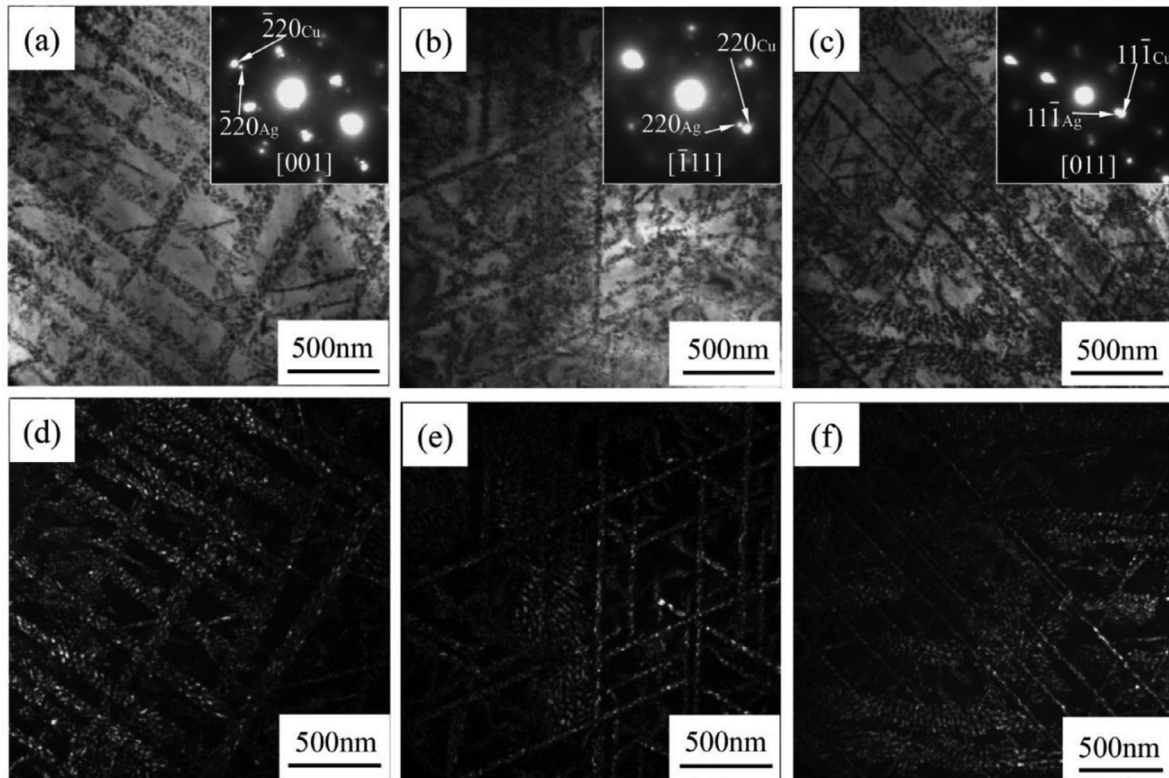


Fig. 6. TEM data showing CPs in a doped sample (0.15 wt%Sc, aged at 450 °C for 2 h). (a, b, and c) Bright-field images of CPs at [001], $[\bar{1}11]$, and [011] zone axis, respectively. SADPs are shown in the insets. (d) Dark field of (a), where the $(220)_{\text{Ag}}$ spot was used to display Ag precipitates. These precipitates are arranged in a checkerboard pattern of perpendicular stripes. (e) Dark field of (b), where the $(220)_{\text{Ag}}$ spot was used to display Ag precipitates, some of which are arranged as interleaved lines at an angle of about 65°, while others are gathered in puddle-like areas. (f) Dark field of (c), where the $(11\bar{1})_{\text{Ag}}$ spot was used to display Ag precipitates, which are arranged in stripes.

during the first 2 h of aging at 450 °C and more rapidly thereafter, from 2 to 16 h (Table 2, Fig. 2(d)). We speculated that the initial slow decrease of lattice constants was the result of slow Ag diffusion rates during the first 2 h when most of the Sc was concentrated at grain boundaries, forming intermetallic compounds with Ag.

In non-doped samples, because of its nucleation site and the higher diffusion rate, DPs nucleated earlier than CPs and grew at a high speed, thus consuming most of the available energy and decreasing the saturation of Ag. Consequently, less energy and dissolved Ag remained for later nucleation of CPs, so only DPs were found in non-doped samples. If these non-doped samples had higher Ag content or had been aged at higher temperatures, enough supersaturated Ag and enough available energy would have remained to allow for nucleation of CPs as well [13].

4.2. Microstructure of deformed samples

Cu/Ag interfaces are typically semi-coherent with multiple misfit dislocations generated by the difference between the lattice parameters of Cu and Ag [54]. When the diameter of Ag fibers is small, some of the lattice plane distances for Ag are so similar to those for Cu that misfit dislocations may appear or disappear at certain zone axes in atomic resolution images. In longitudinal cross-sectional images of the interfaces between the Cu matrix and FCPs whose diameter was as small as 2.5 nm in our doped samples, we found no misfit dislocations in the [011] zone axes perpendicular to the fiber axis (Fig. 13(c)). In transverse cross-sectional images, however, we were able to observe misfit dislocations even though the fiber diameter is only 1.8 nm (Fig. 11(f)). In other words, in the direction parallel to the fiber axis, Cu was in tension and Ag was in compression, whereas in the direction

perpendicular to the fiber axis, the opposite was true, leading to tetragonal lattice distortion in both Cu and Ag [55].

In both non-doped and doped samples, plastic deformation produces stored energy, but only in non-doped samples did this lead to recrystallization of Cu and coarsening of Ag fibers (Fig. 10(c)). In the doped samples (0.15 wt% Sc), however, we observed an emergence of subgrain boundaries, which is a sign of recovery instead of recrystallization (Fig. 12). This may have occurred because the dissolved Sc, whose atom radius is much greater than that of Cu, increased the recrystallization temperature in the doped samples [56].

4.3. Mechanism for suppression of discontinuous precipitation

High-energy grain boundaries are particularly effective nucleation sites for DPs because the higher the energy of the grain boundaries, the lower the nucleation energy needs [22,23]. Critical nucleation energy (W^*) on grain boundaries can be expressed as follows [57]:

$$W^* = \frac{4}{27} \frac{(b\gamma_{\text{AB}} - a\gamma_{\text{AA}})^3}{c^2 \Delta f_v^2} \quad (2)$$

where γ_{AB} is the interfacial energy between Cu matrix and DPs, γ_{AA} is the grain boundary energy, Δf_v is the driving force for nucleation [58]. The coefficients a , b , and c correspond to various types of grain junctions [57].

In doped samples aged for 2 h at 400 °C, we found only CPs. We speculated that the formation of DPs was inhibited by the grain boundary segregation of Sc (Our estimation indicated that the segregated Sc could cover all the grain boundaries, seeing Appendix G). Some segregated Sc and Ag formed thin intermetallic compound layers at grain boundaries (Figs. 4 and 5). Thus, the γ_{AA}

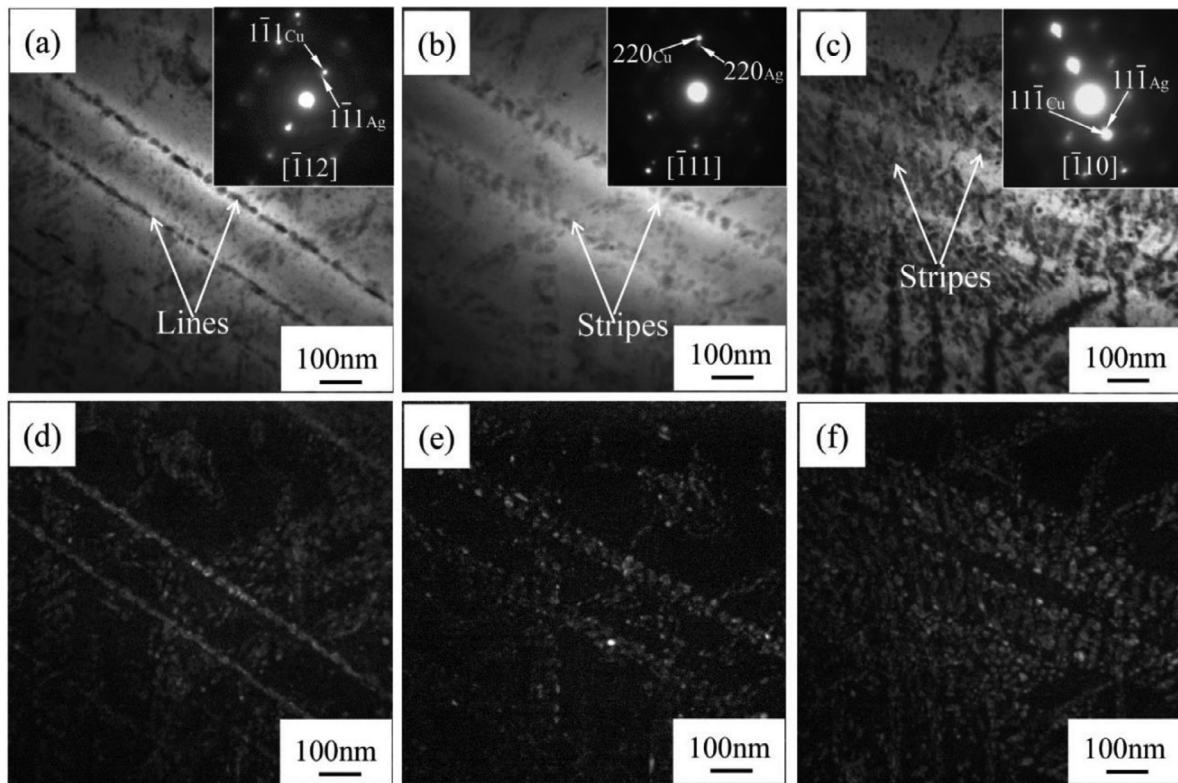


Fig. 7. TEM data showing the changes in the arrangement of CPs that occur in a doped sample (0.15 wt% Sc, aged at 450 °C for 2 h) that is tilted to three different zone axes. (a, b, and c) Bright-field images of CPs at $[\bar{1}12]$, $[\bar{1}11]$, and $[\bar{1}10]$ zone axis, respectively. SADPs are shown in the insets. (d) Dark field image of Fig. (a), where the $(1\bar{1}1)_{Ag}$ spot was used to display CPs that are arranged in two straight lines with a width of 15.0 ± 1.5 nm. (e) Dark field of (b), where the $(220)_{Ag}$ spot was used to display CPs that are arranged in two stripes with a width of 43.6 ± 2.7 nm. (f) Dark field of (c), where the $(11\bar{1})_{Ag}$ spot was used to display CPs in stripes that have widened to 102.3 ± 5.9 nm.

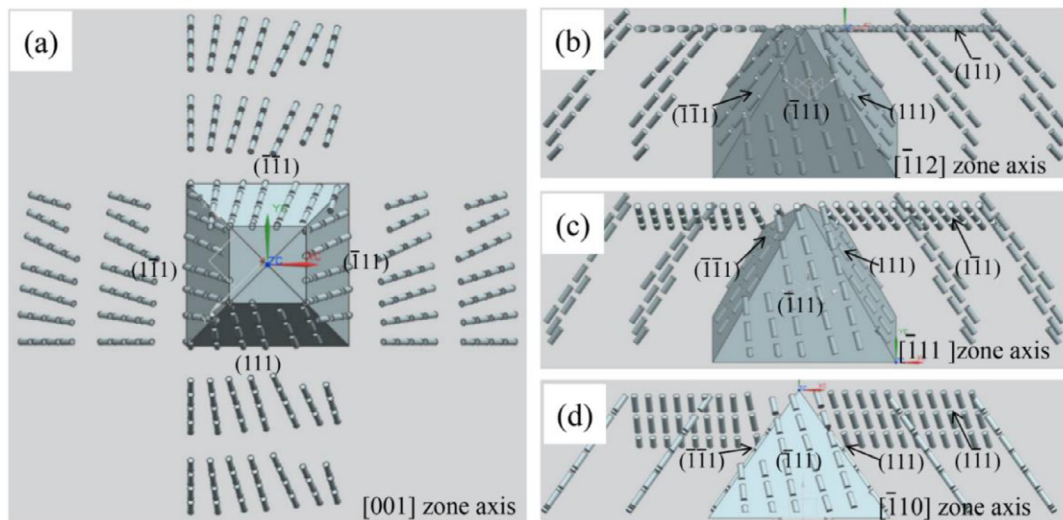


Fig. 8. 3-D model of CPs deduced from the TEM data for doped samples (0.15 wt% Sc, aged at 450 °C for 2 h). (a, b, c, and d) The arrangements of CPs along the $[001]$ zone axis, the $[\bar{1}12]$ zone axis, the $[\bar{1}11]$ zone axis, and the $[\bar{1}10]$ zone axis, respectively. The size of these precipitates, measured from images taken at the $[\bar{1}11]$ zone axis, is $\phi 15.0 \times 42.0$ nm (Fig. 6(b, e)). The distance between Ag lines is 194.8 nm, as measured from the images of $[\bar{1}12]$ zone axis (Fig. 7(a, d)).

in Eq. (2) was replaced by the interface energy between a given Cu grain and the adjacent intermetallic compound (γ_{AC}). Because we did not find any DPs nucleated at the interface between the Cu and the intermetallic compound (Fig. 3(d, e)), we assumed that the value for γ_{AC} was lower than for γ_{AA} . Moreover, some segregated Sc atoms might not form the intermetallic compound but were free

at grain boundaries. This segregating solute is known to inhibit grain boundary diffusion and reduce γ_{AA} [29,31]. Consequently, Sc segregation at Cu grain boundaries would likely suppress nucleation of DPs by increasing W^* and decreasing the diffusion rate of Ag. In addition, Sc-rich precipitates may provide nucleation sites for CPs, reducing the nucleation barrier.

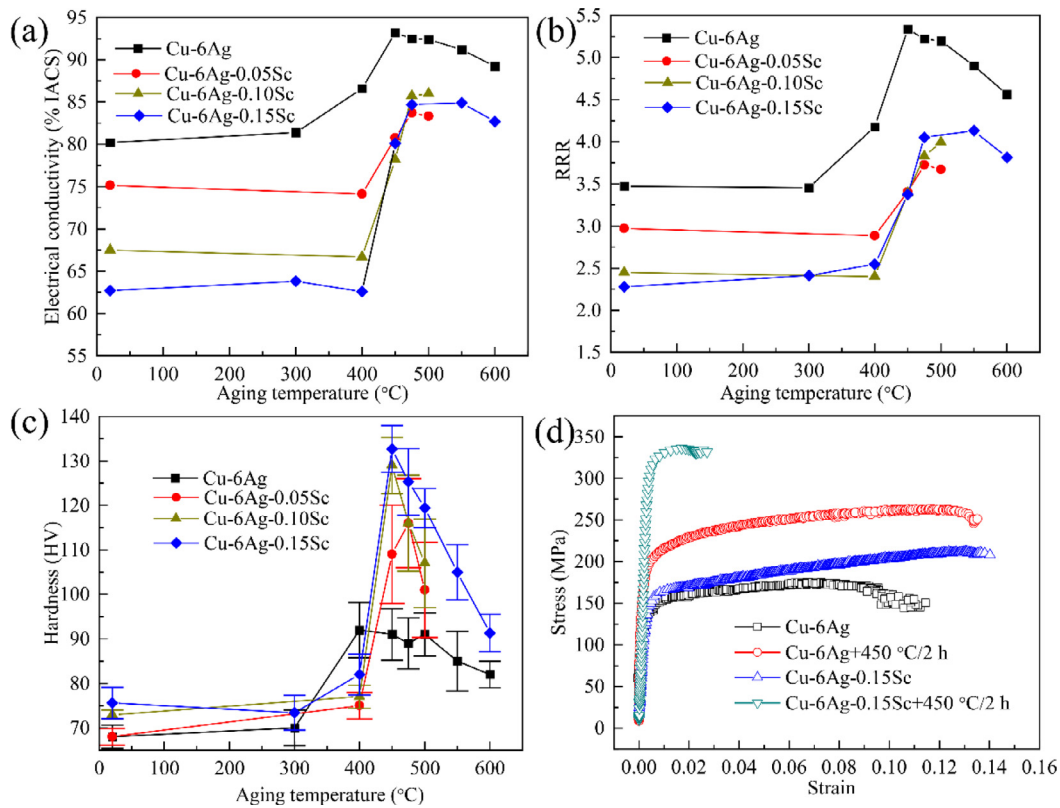


Fig. 9. Properties of non-doped and doped samples aged for 2 h at various temperatures. (a) Electrical conductivity. (b) RRR. (c) Hardness. (d) Stress–strain curves.

Grain boundary segregation ratio (s) can be expressed as follows [59]:

$$s = s_0 \exp\left(\frac{-\Delta H_i^{GB}}{RT}\right) \quad (3)$$

where s_0 is the pre-exponential factor, ΔH_i^{GB} is the segregation enthalpy, R is the gas constant, and T is the absolute temperature. In Cu-Ag alloys, s is 25.9 after aging at 402 °C [59]. Previous research has shown that lower bulk solubility leads to higher grain boundary segregation [60,61]. The solubility of Sc in Cu is much lower than that of Ag in Cu (0.04 at% as opposed to 0.12 at% at room temperature [38,45]). Thus, Sc has higher s than Ag, indicating that segregated Sc in our doped samples may have reduced segregation of Ag at grain boundaries.

In the doped samples that had been aged at higher temperatures (450 °C, 500 °C), we observed some DPs near grain boundaries. We attribute this phenomenon to (1) a lower value for s at higher temperature (Eq. (3)), indicating the presence of less Sc at grain boundaries, and (2) a higher moving speed of the reaction front. The growth of DPs, however, might have been suppressed by the consumption of supersaturated Ag by CPs and the drag on reaction fronts introduced by the concentration of both CPs and dissolved Sc at interface boundaries [26,27,62].

We assumed that when grain boundaries were occupied by other species rather than whatever elements to form discontinuous precipitates, the discontinuous precipitation would be inhibited. For example, discontinuous precipitates in Cu-25 wt%Ag were suppressed because eutectics occupied the grain boundaries [14]. When some new grain boundaries formed in the Cu matrix by triggering recrystallization, discontinuous precipitates nucleated [14]. In Cu-7 wt%Ag, doping with 0.05 wt%Zr also inhibited discontinuous precipitation [36]. Although the particular reason was not claimed by the authors, we suspected it was the Zr-segregation that caused a decrease in grain boundary energy because Zr had

little solubility in Cu at room temperature [39,60]. This suppression mechanism was also discussed in multicomponent U-10Mo alloys and NiAl-strengthened steels [26,63]. We believe this mechanism can help others to find the proper elements to suppress discontinuous precipitation in other alloys.

4.4. Strengthening mechanisms

Precipitation hardening (σ_p) from DPs and CPs can be calculated using the Orowan–Ashby equation [64]:

$$\sigma_p = \frac{0.84M(1.2G_{\text{mix}}b_{\text{Cu}})}{2\pi\lambda_p} \ln \frac{r}{b_{\text{Cu}}} \quad (4)$$

where M is the Taylor factor for polycrystalline materials (3.0 [65]), G_{mix} is the shear modulus of Cu (G_{Cu} : 45 GPa), b_{Cu} is the Burgers vector of Cu (0.2556 nm [66]), λ_p is the spacing between precipitates in the slip planes ($\{111\}$ for Cu), and r is the average radius of precipitates. In the non-doped sample, we used the λ_p and the r obtained from SEM images because there was no particular habit plane for DPs [67]. In that case, λ_p was 160.0 ± 60.0 nm and r was 15.1 ± 3.7 nm (Fig. 3(b)). In the doped sample, λ_p was 66.4 ± 19.0 nm, and r was 7.5 ± 0.8 nm, as measured from TEM images taken at the $[111]$ zone axis (Fig. 6(b, e)). We found that the strength produced by CPs was 282 MPa, which is twice the strength produced by DPs (141 MPa).

When ε was at 4.9, both DPs and CPs were drawn into fibers, significantly increasing the tensile strength of Cu-Ag. The Hall–Petch model [50,68–70], which is generally used to calculate the yield strength of polycrystalline single-phase metals and is often extended to filamentary alloys, can also be used to calculate the yield strength of Cu-Ag alloys ($\sigma_{\text{Cu-Ag}}$). It can be expressed as follows:

$$\sigma_{\text{Cu-Ag}} = \sigma_{0\text{Cu}} + k_{\text{Cu/Ag}}\lambda_f^{-1/2} \quad (5)$$

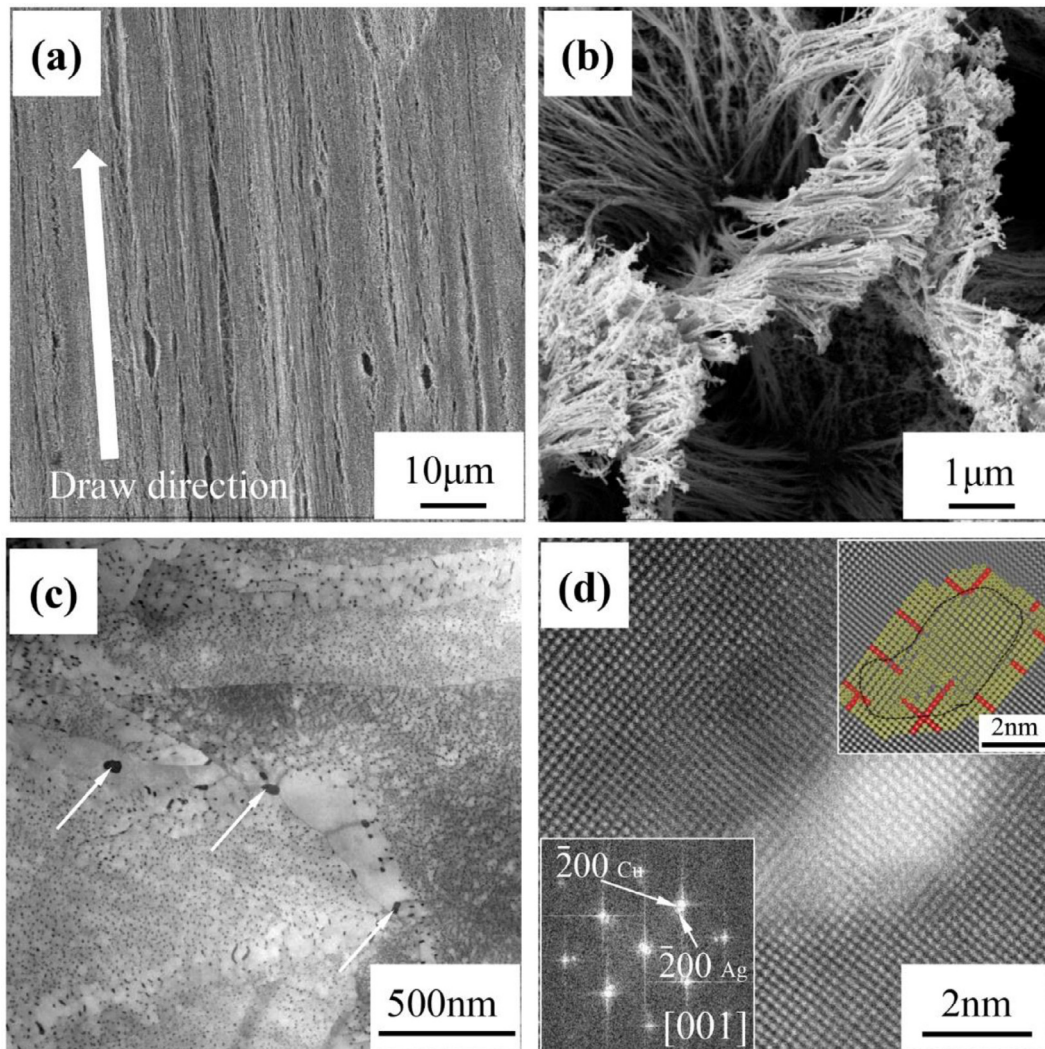


Fig. 10. Images showing FDPs in non-doped samples with $\varepsilon = 4.9$: (a, b) SEM images, (c, d) STEM images. (a) SEM image of FDPs in longitudinal cross-section. (b) SEM image of FDPs in transverse cross-section. (c) Bright-field STEM (BF-STEM) image of FDPs in transverse cross-section, showing coarsened FDPs (white arrows) among recrystallized Cu grains. (d) HAADF image of one Ag fiber (light contrast) in Cu matrix. Left-bottom inset is the FFT image, showing that the zone axis is [001]. Right-top inset is the Inverse Fast Fourier Transform (IFFT) image, showing the Ag fiber (outlined in black), surrounded by misfit dislocations (marked by red circles).

where σ_{0Cu} , which combines solid-solution hardening and grain-boundary hardening, is the yield stress of polycrystalline Cu. $k_{Cu/Ag}$ is the Hall–Petch constant of a deformed Cu–Ag alloy.

As far as we know, the $k_{Cu/Ag}$ of deformed Cu–6 wt%Ag alloy has not yet been reported, so we explored whether the Hall–Petch model, using a constant $k_{Cu/Ag}$, could be effectively used to analyze the strength of Cu–6wt%Ag samples with different Ag fiber spacing. To do so, we calculated the $k_{Cu/Ag}$ of deformed Cu–24 wt%Ag from Frommeyer’s data using Eq. (5), assuming that the yield strength was the same as the ultimate tensile strength and omitting the σ_{0Cu} because of its small contribution [51,68,71]. When λ_f was more than 60 nm, the resulting $k_{Cu/Ag}$ was as high as 0.24 MPa $m^{1/2}$. As λ_f continued to decrease, however, the $k_{Cu/Ag}$ also decreased, reaching 0.16 MPa $m^{1/2}$ when λ_f reached 13 nm (Fig. 15). In other words, the Hall–Petch model failed to accurately calculate strength with a constant $k_{Cu/Ag}$ when λ_f fell below 60 nm in Cu–24 wt%Ag. The Hall–Petch model is based on two assumptions: (1) the spacing of obstacles is sufficiently large to allow dislocations to pile up before slipping past the obstacles, and (2) the strength of such obstacles does not change even when their spacing decreases [72]. Both assumptions, however, break down at nanometer scale. In small spaces, dislocation pileups are much less likely to occur

[73,74]. Moreover, the strength of the obstacles, i.e., their interface barrier strength, is no longer a constant at nanometer scale [72].

When our Cu–6wt%Ag samples reached maximum strain at 4.9, interface spacing of non-doped and doped samples were only about 43.3 nm and 25.6 nm, respectively, much lower than the critical Ag fiber spacing in Cu–24 wt%Ag that rendered the $k_{Cu/Ag}$ useless for calculating strength. The fiber diameter of non-doped and doped samples was about 3.2 nm and 1.8 nm, respectively, which would change the spacing of misfit dislocations on Cu/Ag interfaces enough to introduce an extra strengthening effect as the result of internal stress [75,76].

4.5. Electrical conductivity

Matthiessen’s rule states that the resistivity of an alloy, such as Cu–Ag (ρ_{Cu-Ag}), is a combination of phonon interactions (ρ_{pho}), defects (ρ_{def}), and impurities (ρ_{imp}) [77]:

$$\rho_{Cu-Ag} = \rho_{pho} + \rho_{def} + \rho_{imp} \quad (6)$$

The value of ρ_{pho} is related to temperature. The value of ρ_{def} is related to the density of dislocations (ρ_{dis}), vacancies (ρ_{vac}), grain boundaries (ρ_{GB}), and interfaces (ρ_{int}). The value of ρ_{imp} is related

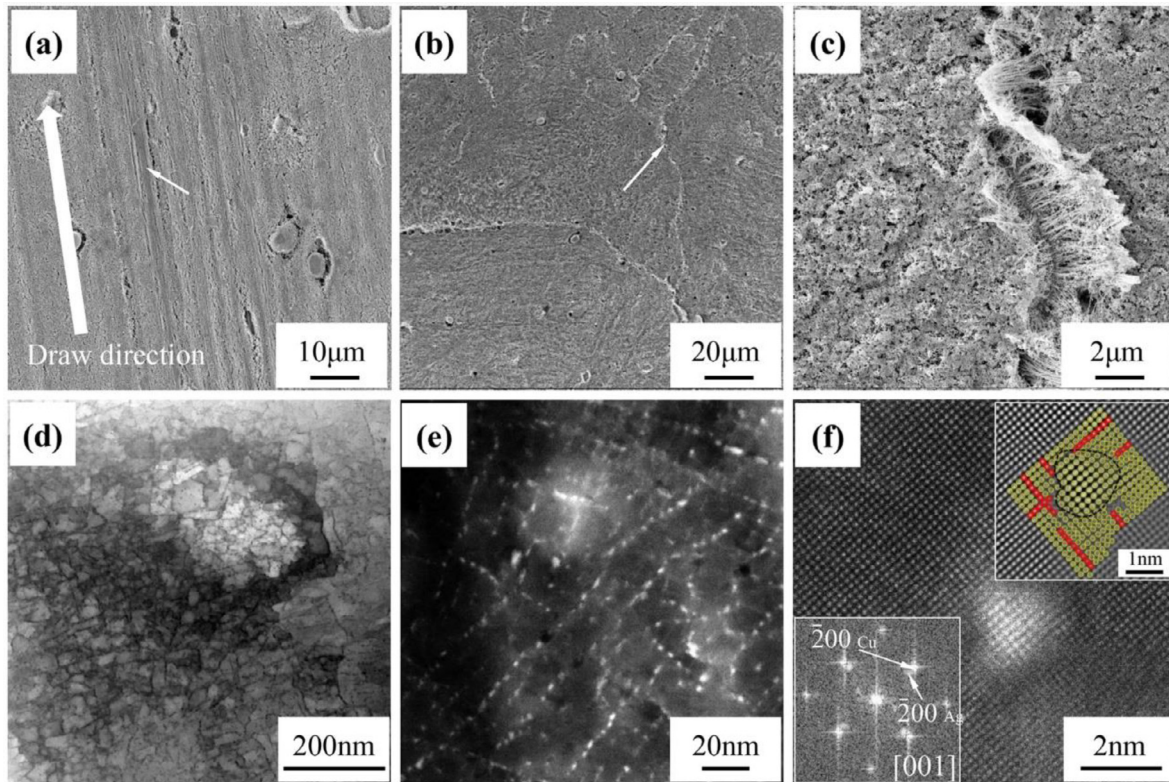


Fig. 11. Images of both FDPs and FCPs in doped samples (0.wt%Sc) with $\varepsilon = 4.9$: (a) SEM image of Ag fibers in longitudinal cross-section. The FDPs are marked by white arrows. (b) SEM image of Ag fibers in transverse cross-section. The FDPs are marked by white arrows. (c) High magnification SEM image of the Ag fibers from (b). We used STEM instead of SEM to reveal the detailed structure of FCPs because TEM/STEM has significantly high resolution and can provide more crystallographic information. (d) BF-STEM image in transverse cross-section of FCPs. (e) High-magnification HAADF-STEM image of FCPs in transverse cross-section, showing the FCPs arranged in lines. (f) HAADF-STEM image in transverse cross-section of one Ag fiber from FCPs. The white dots are the tops of the columns of Ag atoms. The left-bottom inset is the FFT image, showing that the zone axis is [001]. The right-top inset is the IFFT image, showing the Ag fiber outlined in black and surrounded by misfit dislocations (marked by red circles). The fiber diameter is around 1.8 nm.

Table 5

Calculated resistivity of non-doped and doped samples (0.15 wt% Sc) aged for 2 h at 450 °C at 22 °C and -196 °C.

Resistivity	Non-doped samples ($\mu\Omega$ cm)		Doped samples ($\mu\Omega$ cm)	
	22 °C	-196 °C	22 °C	-196 °C
ρ_{imp}	0.18	0.18	0.46*	0.39*
ρ_{pho}	1.70	0.20	1.70	0.20
Calculation	1.88 (91.7% IACS)	0.38	N/A	N/A
Experiment	1.85 (93.2% IACS)	0.35	2.16 (79.9% IACS)	0.59

* ρ_{imp} in the doped samples was calculated with experimental data.

to the fraction of solute in solid solution. In all samples before deformation, ρ_{def} was not considered because in those samples, the density of ρ_{dis} , ρ_{vac} , ρ_{GB} , and ρ_{int} was insignificant.

ρ_{pho} for a defect-free alloy in Cu-Ag, is a combination of the resistivity values of pure Cu and pure Ag. For calculation, we used the following parameters: ρ_{pho} of Cu at 22 °C and at -196 °C is equal to 1.70 $\mu\Omega$ cm and 0.20 $\mu\Omega$ cm, respectively; ρ_{pho} of Ag at 22 °C and at -196 °C is equal to 1.61 $\mu\Omega$ cm and 0.30 $\mu\Omega$ cm, respectively [78,79]. ρ_{imp} depends on the concentration of impurity, and can be calculated as follows:

$$\rho_{imp} = N X_a \quad (7)$$

where N is the Nordheim coefficient. It is 0.123 $\mu\Omega$ cm/at.% for Ag in Cu [80,81].

The resistivity of both non-doped and doped samples aged at 450 °C for 2 h was calculated at 22 °C and -196 °C (Table 5). These calculated resistivity values were very similar to the resistivity value that we measured in the non-doped samples. Because

Table 6

Mean free path of conduction electrons (l_0) for pure Cu and Ag at 22 °C and -196 °C.

	l_0 for pure Cu (nm)	l_0 for pure Ag (nm)
Temperature		
22 °C	38.7	52.3
-196 °C	328.7	280.8

x_a of the doped samples could not be calculated using XRD results, ρ_{imp} was calculated using the measured resistivity values. The value for ρ_{imp} was higher in the doped samples than in the non-doped samples. There are three possible reasons for the difference: (1) the lower diffusion rate of Ag in doped samples may have caused more Ag to accumulate in the Cu matrix, (2) a very small amount of Sc may have remained in the Cu matrix, or (3) the smaller size of the Ag particles in the doped samples may have allowed more Ag to dissolve into the Cu matrix (Gibbs-Thomson effect [82]).

Since the deformation strain increased, the electrical conductivity of both non-doped and doped samples decreased. The value for ρ_{imp} in the deformed samples was assumed to be the same as in the corresponding undeformed samples. Using Eq. (6), we calculated the ρ_{imp} of the non-doped and doped samples aged at 450 °C for 8 h as 0.16 $\mu\Omega$ cm and 0.25 $\mu\Omega$ cm, respectively (ρ_{Cu-Ag} of the non-doped and doped samples at 22 °C was 1.86 $\mu\Omega$ cm and 1.95 $\mu\Omega$ cm (94.2% IACS and 88.1% IACS as shown in Fig. 14(a)), respectively, and ρ_{pho} at 22 °C was 1.70 $\mu\Omega$ cm).

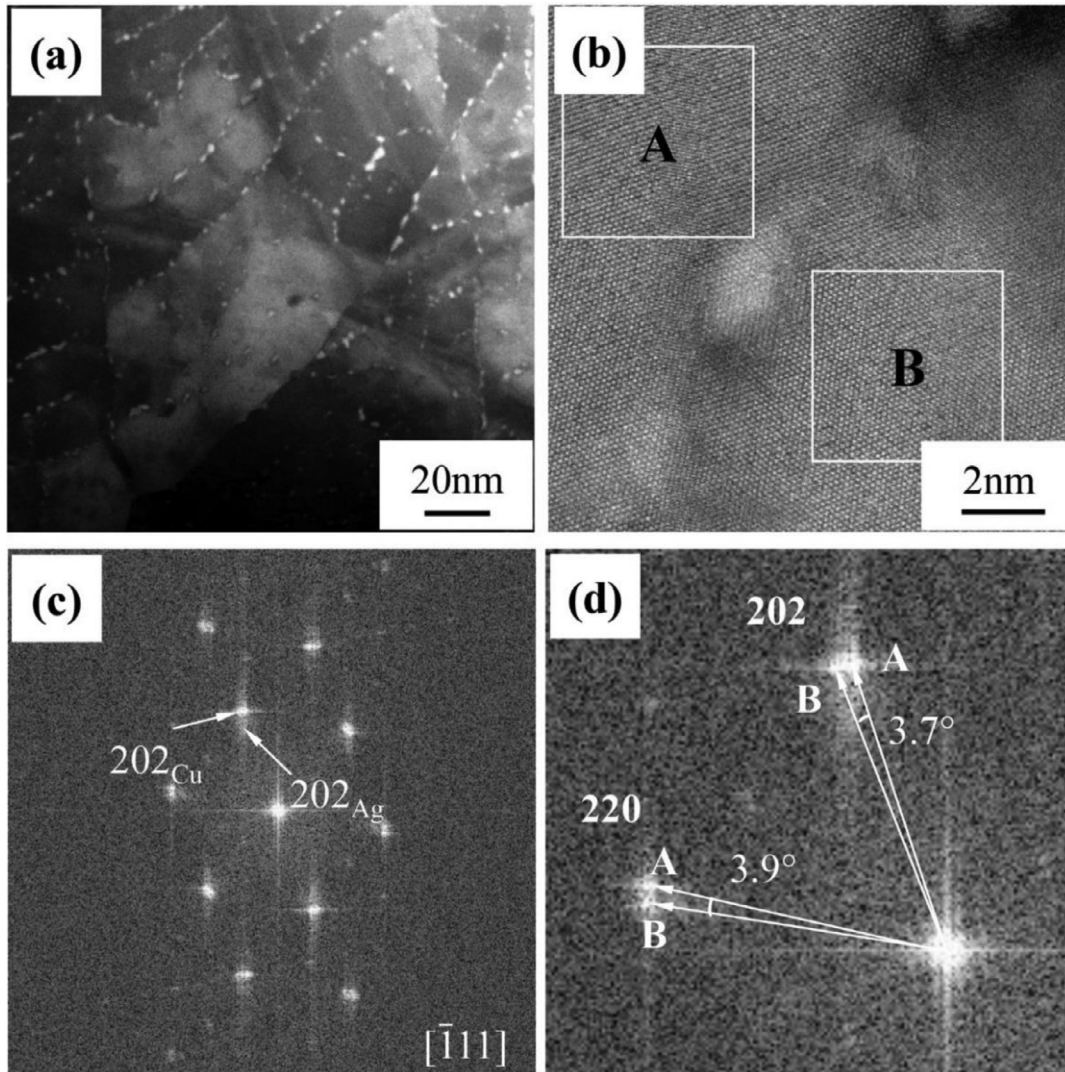


Fig. 12. HAADF-STEM images in transverse cross-section of subgrain boundaries in doped samples (0.15 wt% Sc) with $\varepsilon = 4.9$: (a) Ag fibers (white dots) along the boundaries. (b) High-magnification image of the grains (A and B) next to a boundary. (c) FFT image of (b). (d) Enlargement of (c). The dots marked in A and B are the diffraction patterns of areas A and B in (b).

The density of dislocations increased considerably after deformation, but the effect of dislocations on resistivity was very small, only around 2.8×10^{-13} and $1.6 \times 10^{-13} \mu\Omega \text{ cm}$ per dislocation line/cm² at 0 °C and -196 °C, respectively [83,84]. In previous research, the dislocation density of Cu matrix in Cu-Nb composites has maintained a saturated value around $4 \times 10^{10} \text{ cm}^{-2}$ at strains ranging from 3.6 to 6.9 [85,86]. At this dislocation density, ρ_{dis} would be only around 0.01 and 0.006 $\mu\Omega \text{ cm}$ at 0 °C and -196 °C, respectively. We speculated that the dislocation density in our samples would remain at a level of $4 \times 10^{10} \text{ cm}^{-2}$ at a deformation strain of 4.9, thus we omitted ρ_{dis} . The ρ_{pho} was the same in both undeformed and deformed samples. ρ_{CB} was very small and was neglected here [85,87–89].

ρ_{int} increased considerably because Cu-Ag was divided into numerous Cu channels and Ag channels by Cu/Ag interfaces. The resistivity produced by Cu/Ag interfaces (ρ_{int}) can be calculated with the Dingle model [80,90,91]:

$$\rho_{\text{int}} = \rho_0 \left(\frac{(1-p)}{(1+p)} \frac{l_0}{d_{\text{Ch}}} - 1 \right), \quad \left(\frac{l_0}{d_{\text{Ch}}} \gg 1 \right) \quad (8)$$

$$\rho_{\text{int}} = \rho_0 \left(\frac{3}{4} (1-p) \frac{l_0}{d_{\text{Ch}}} \right), \quad \left(\frac{l_0}{d_{\text{Ch}}} \ll 1 \right) \quad (9)$$

where ρ_0 is the resistivity for Cu or Ag without defects, which is the same as the values of their ρ_{pho} . p is the probability of elastic scattering at the phase boundary. The value for d_{Ch} is the diameter of each phase channel. l_0 is equivalent to the mean free path of the conduction electrons. In Cu-Ag alloys, the values of p are 0.81 and 0.84 at 25 °C and -196 °C, respectively [87,88]). The diameter of Cu channels is equivalent to the mean random edge-to-edge distance of Ag fibers (λ_f). The diameter of Ag channels is equivalent to the diameter of Ag fibers (d_{Ag}). The values for l_0 in Cu and in Ag at 22 °C and at -196 °C were shown in Table 5 (The calculation process was shown in Appendix H).

In both non-doped and doped samples at $\varepsilon = 4.9$, the values of l_0/d_{Ch} of Cu and Ag phases were calculated and shown in Table 7. They were not much less or greater than 1. Therefore, it was inaccurate to use the Eqs. (8) and (9) to calculate ρ_{int} . When $0.1 \leq l_0/d_{\text{Ch}} \leq 1000$, Sambles and Preist [91] proposed a model, which was shown as follows:

$$\rho_{\text{int}} = \rho_0 \alpha \left(\frac{l_0}{d_{\text{Ch}}} \right)^n, \quad (0.1 \leq \frac{l_0}{d_{\text{Ch}}} \leq 1000) \quad (10)$$

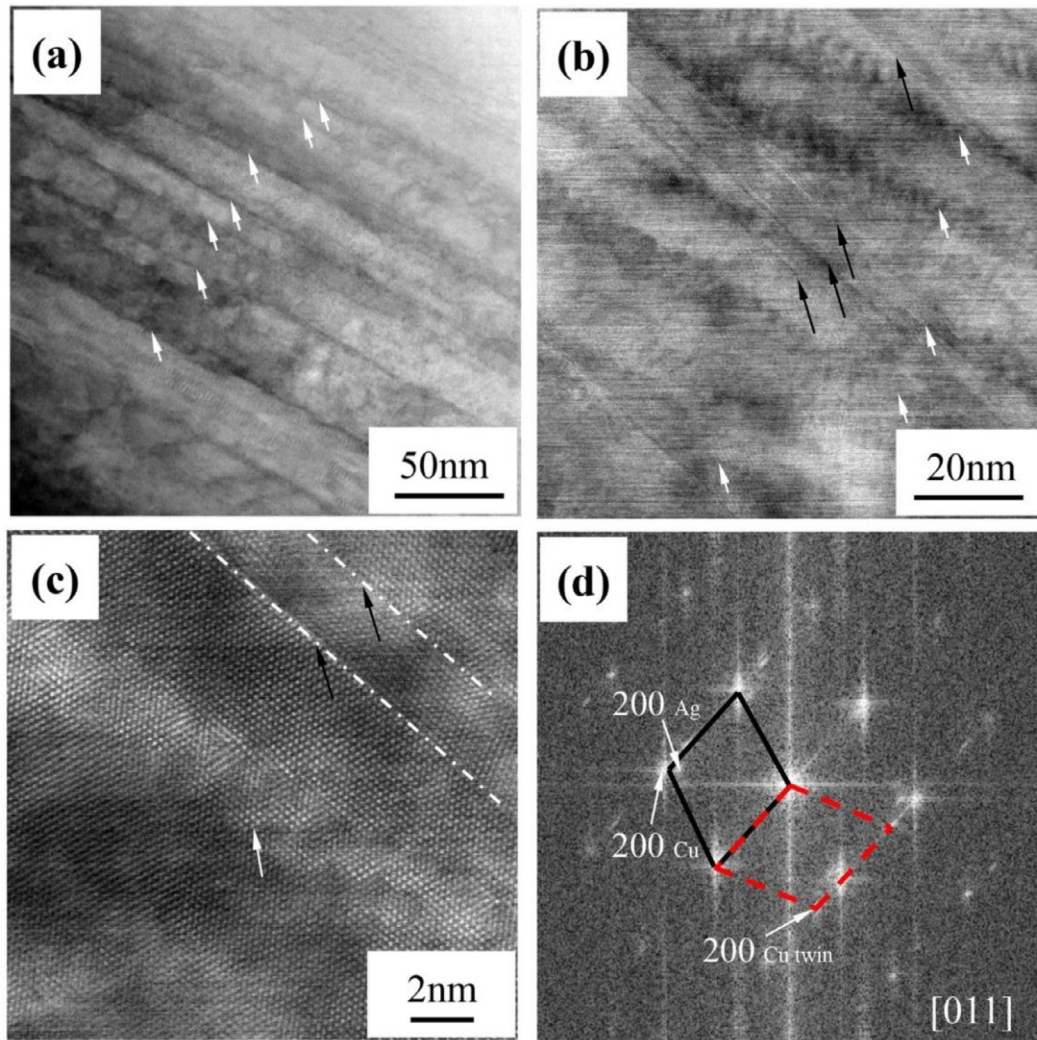


Fig. 13. STEM images in longitudinal cross-section of Ag fibers in doped samples (0.15 wt% Sc) with $\epsilon = 4.9$: (a) BF-STEM image of Ag fibers (indicated by small white arrows). (b) BF-STEM image of Ag fibers (white arrows) and twins (black arrows). (c) High magnification HAADF-STEM image of Ag fibers (one of which is indicated by a white arrow) and twin boundaries (black arrows). The fiber diameter is around 2.5 nm. (d) FFT image of the area from (c), showing twins in Cu matrix. Diffraction spots from the matrix are connected by solid black lines, from the twins by red dashed lines.

Table 7

l_0/d_{Ch} of Cu and Ag phase in non-doped and doped samples (0.15 wt% Sc) at 22 °C and -196 °C when $\epsilon = 4.9$.

	Cu channel		Ag channel	
	22 °C	-196 °C	22 °C	-196 °C
Non-doped	0.89	7.59	16.34	87.75
Doped	1.49	12.69	29.06	156.00

where α and n are functions of l_0/d_{Ch} . Their values, however, are different in different small ranges of l_0/d_{Ch} , making it impossible to use Eq. (10) to calculate ρ_{int} .

After deformation, Cu channels are aligned parallel to Ag fibers. They can be treated as parallel-connected resistors. Therefore, the resistivity of Cu-Ag alloys ($\rho_{deformed\ Cu-Ag}$) can be calculated as follows [92,93]:

$$\frac{1}{\rho_{deformed\ Cu-Ag}} = \frac{f_{Cu}}{\rho_{Cu}} + \frac{f_{Ag}}{\rho_{Ag}} \quad (11)$$

where f_{Ag} is the volume fraction of the Ag phase. The value for f_{Cu} is equivalent to $1 - f_{Ag}$. The f_{Ag} is only about 4.6% in non-doped and doped samples, which causes that the value of ρ_{Ag} has a slight effect on $\rho_{deformed\ Cu-Ag}$ (see Appendix I). Therefore, we omitted

Table 8

Interfacial scattering (ρ_{int}) for Cu and Ag in non-doped and doped samples (0.15 wt%Sc) at 22 °C and -196 °C when $\epsilon = 4.9$.

	Temperature	Temperature	
		22 °C	-196 °C
Non-doped sample	$\rho_{deformed\ Cu-Ag}$ ($\mu\Omega\ cm$)	2.18	0.68
	ρ_{pho} ($\mu\Omega\ cm$)	1.70	0.20
	ρ_{imp} ($\mu\Omega\ cm$)	0.16	0.16
	ρ_{int} ($\mu\Omega\ cm$)	0.32	0.32
Doped sample	$\rho_{deformed\ Cu-Ag}$ ($\mu\Omega\ cm$)	2.59	1.03
	ρ_{pho} ($\mu\Omega\ cm$)	1.70	0.20
	ρ_{imp} ($\mu\Omega\ cm$)	0.25	0.25
	ρ_{int} ($\mu\Omega\ cm$)	0.64	0.58

the resistivity of ρ_{Ag} and calculated the ρ_{int} with Eq. (6) (Table 8). In doped samples, because of the thinner channels of Cu, the value for ρ_{int} in Cu was around 2 times the values in non-doped samples. Consequently, doped samples had lower electrical conductivity and RRR.

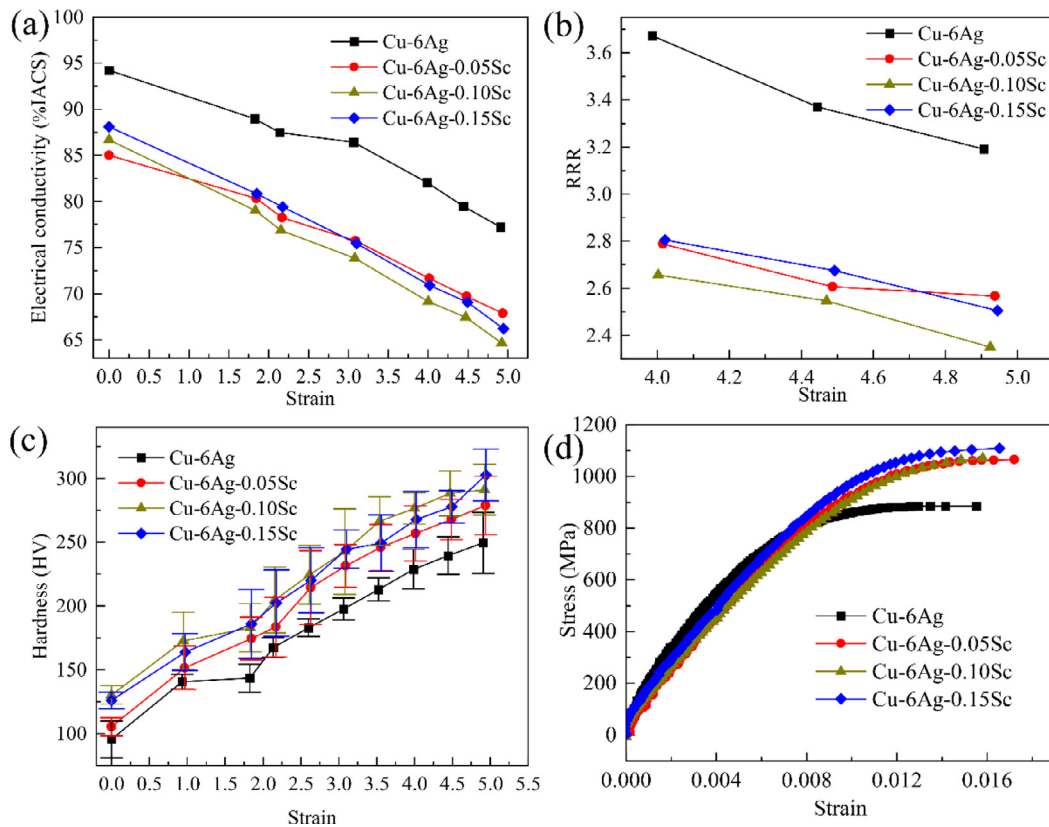


Fig. 14. Effect of strain levels on the properties of non-doped and doped samples. (a) Electrical conductivity. (b) RRR. (c) Hardness. (d) Strain-stress curves of samples at $\varepsilon = 4.9$.

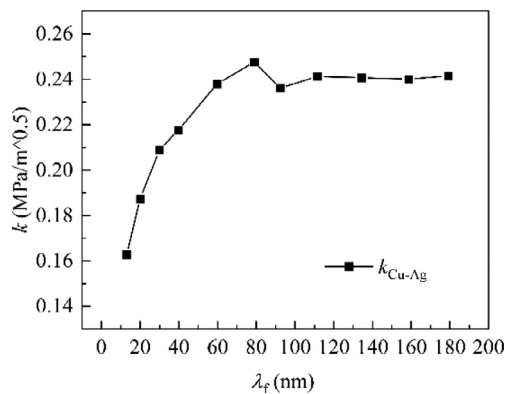


Fig. 15. Calculated value of $k_{\text{Cu/Ag}}$ for deformed Cu-24 wt%Ag, derived from data collected by Frommeyer and Wassermann [71].

4.6. Comparison between our work and previous research

We measured UTS and electrical conductivity in non-doped and doped samples deformed to a strain of 4.9. When we compared these values to those reported by other researchers, we found that our non-doped samples were similar to the Cu-6 wt%Ag samples of others. For a combination of UTS and electrical conductivity, our doped samples performed better than Cu-6 wt%Ag, Cu-6 wt%Ag-0.5 wt%Cr, Cu-6 wt%Ag-RE, and Cu-6 wt%Ag-0.2 wt%Zr, similar to the properties of Cu-24 wt%Ag [8,33,34,94] (Fig. 16). Some previous researchers used intermediate aging treatments, which were reported to benefit strength and electrical conductivity [95,96]. We assume that the properties of our samples could be further improved with appropriate intermediate aging treatments between

deformations. With the advantages of ingot fabrication and the high strength and high conductivity, Cu-6 wt%Ag-Sc alloys can be sufficient to manufacture wires for high-field magnets.

5. Conclusion

- (1) In non-doped samples, aging produced only discontinuous precipitates, but in doped samples, most areas were filled with continuous precipitates after aging, although some discontinuous precipitates remained, mostly near grain boundaries. We concluded that doping with Sc significantly suppressed discontinuous precipitates.
- (2) Doping decreased electrical conductivity only slightly in aged samples, but because of the high-volume percentage of continuous precipitates, which were arranged on {111} plane, doping increased strength in aged samples by 55 MPa.
- (3) In doped samples, Ag and Sc were concentrated at grain boundaries, where they formed thin intermetallic compound layers, converting high-energy grain boundaries into low-energy interfaces, thus erasing preferred nucleation sites for the discontinuous precipitates, which had previously depended on high-energy grain boundaries for a critical part of their nucleation energy.
- (4) Discontinuous precipitates, which nucleated on grain boundaries and thus required lower activation energy, were governed by Ag interface diffusion. Continuous precipitates, which nucleated inside grains and thus required higher activation energy, were governed by Ag volume diffusion.
- (5) After deformation, the electrical conductivity of all samples decreased, while the hardness increased. At a strain of 4.9, electrical conductivity decreased to around 66% IACS for doped and 77% IACS for non-doped samples. The hardness increased to 290 HV for doped and 249 HV for non-doped samples. The av-

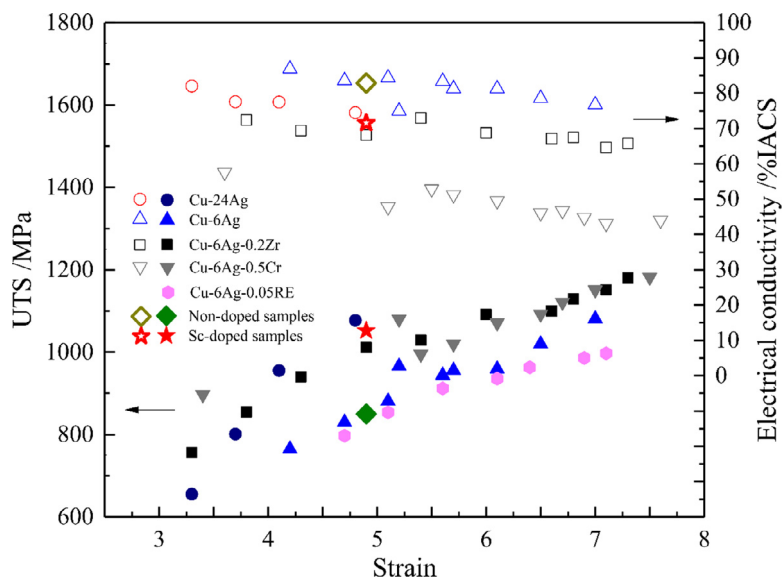


Fig. 16. Comparison of data from our research and that of other's [8,33,34,94]. Outlined symbols and solid symbols show the electrical conductivity and the UTS, respectively.

verage UTS of doped samples was 1080 MPa, 205 MPa higher than the average of non-doped samples.

- (6) In doped samples subjected to a deformation strain of 4.9, we did not observe any misfit dislocations on the longitudinal cross-section, but we found numerous misfit dislocations on the transverse cross-section, indicating lattice distortion.
- (7) In all samples, strength was attributable to the refinement of Ag fiber spacing after deformation. Narrower fiber spacing led to higher strength. Electrical conductivity decreased considerably because of an increase in interface scattering stemming from the narrowness of Ag fiber spacing and the thinness of Ag fibers.

Acknowledgments

This work was supported by the National Key R&D Program of China (No. 2017YFE0107900) and the 111 Project (2.0) of China (No. BP0719037). Some work was performed at the National High Magnetic Field Laboratory, USA, which is supported by the National Science Foundation Cooperative Agreement (Nos. DMR-1157490 and NSF DMR-1644779) and the State of Florida, USA. The authors are grateful to Mary Tyler for editing. The authors are grateful to China Scholarship Council (CSC) for financial support.

Supplementary materials

Supplementary material associated with this article can be found, in the online version, at doi:10.1016/j.jmst.2022.06.043.

Reference

- [1] K. Han, A. Baca, H. Coe, J. Embury, K. Kihara, B. Lesch, L. Li, J. Schillig, J. Sims, S.V. Sciver, H.J. Schneider-Muntau, *IEEE Trans. Appl. Supercond.* 10 (2000) 1277–1280.
- [2] K. Han, J. Lu, V. Toplosky, R.M. Niu, R. Goddard, Y. Xin, R. Walsh, I. Dixon, V. Pantisyrny, *IEEE Trans. Appl. Supercond.* 30 (2020) 1–5.
- [3] Y. Sakai, H.J. Schneider-Muntau, *Acta Mater.* 45 (1997) 1017–1023.
- [4] P.S. Chen, J.H. Sanders, Y.K. Liaw, F. Zimmermann, *Mater. Sci. Eng. A* 199 (1995) 145–152.
- [5] J.H. Sanders, P.S. Chen, S.J. Gentz, R.A. Parr, *Mater. Sci. Eng. A* 203 (1995) 246–255.
- [6] X. Wu, R.C. Wang, C.Q. Peng, X.F. Wang, *J. Alloy. Compd.* 828 (2020) 154371.
- [7] K. Han, V.J. Toplosky, Y. Xin, J.R. Sims, C.A. Swenson, *IEEE Trans. Appl. Supercond.* 20 (2011) 1463–1466.
- [8] K. Han, J.D. Embury, J.R. Sims, L.J. Campbell, H.J. Schneider-Muntau, V.I. Pantisyrny, A. Shikov, A. Nikulin, A. Vorobieva, *Mater. Sci. Eng. A* 267 (1999) 99–114.
- [9] C.A. Davy, K. Han, P.N. Kalu, S.T. Bole, *IEEE Trans. Appl. Supercond.* 18 (2008) 560–563.
- [10] A. Gaganov, J. Freudenberger, W. Grünberger, L. Schultz, *Z. Metallkd.* 95 (2004) 425–432.
- [11] X.W. Zuo, R. Guo, C.C. Zhao, L. Zhang, E.G. Wang, K. Han, *J. Alloy. Compd.* 676 (2016) 46–53.
- [12] A. Benghalem, D.G. Morris, *Acta Mater.* 45 (1997) 397–406.
- [13] C.C. Zhao, X.W. Zuo, E.G. Wang, R.M. Niu, K. Han, *Mater. Sci. Eng. A* 652 (2016) 296–304.
- [14] W. Grünberger, M. Heilmaier, L. Schultz, *Z. Metallkd.* 93 (2002) 58–65.
- [15] D. Hamana, M. Hachouf, L. Boumazza, Z.E.A. Biskri, *Mater. Sci. Appl.* 2 (2011) 899–910.
- [16] J.B. Liu, L. Meng, *J. Mater. Sci.* 43 (2008) 2006–2011.
- [17] B.L. An, Y. Xin, R.M. Niu, Z.L. Xiang, E.G. Wang, K. Han, *Mater. Res. Express* 9 (2022) 026530.
- [18] Y. Sakai, K. Inoue, H. Maeda, *IEEE Trans. Magn.* 30 (1994) 2114–2117.
- [19] I. Manna, *Interface Sci.* 6 (1998) 113–131.
- [20] B.L. An, Y. Xin, R.M. Niu, Z.L. Xiang, Y.F. Su, J. Lu, E.A. Wang, K. Han, *Mater. Charact.* 189 (2022) 111965.
- [21] I. Manna, S.K. Pabi, W. Gust, *Int. Mater. Rev.* 46 (2001) 53–91.
- [22] R. Monzen, H. Shigehara, K. Kita, *J. Mater. Sci.* 35 (2000) 5839–5843.
- [23] R. Monzen, C. Watanabe, D. Mino, S. Saida, *Acta Mater.* 53 (2005) 1253–1261.
- [24] N.A. Gjostein, F.N. Rhines, *Acta Metall.* 7 (1959) 319–330.
- [25] K. Han, J.P. Hirth, J.D. Embury, *Acta Mater.* 49 (2001) 1537–1540.
- [26] A. Devaraj, L. Kovarik, E. Kautz, B. Arey, S. Jana, C. Lavender, V. Joshi, *Acta Mater.* 151 (2018) 181–190.
- [27] I. Manna, S.K. Pabi, *Phys. Status Solidi A* 123 (1991) 393–398.
- [28] D.B. Williams, E.P. Butler, *Int. Met. Rev.* 26 (1981) 153–183.
- [29] H. Sautter, H. Gleiter, G. Bäro, *Acta Metall.* 25 (1977) 467–473.
- [30] E. Hornbogen, *Metall. Mater. Trans. B* 3 (1972) 2717–2727.
- [31] J. Bernardini, P. Gas, E.D. Hondros, M.P. Seah, R.B. Nicholson, *Proc. R. Soc. A* 379 (1982) 159–178.
- [32] X.W. Zuo, J.Z. Zhu, B.L. An, K. Han, R. Li, E.G. Wang, *Met. Mater. Int.* 23 (2017) 974–983.
- [33] L. Zhang, L. Meng, J.B. Liu, *Scr. Mater.* 52 (2005) 587–592.
- [34] J.B. Liu, L. Zhang, L. Meng, *Mater. Sci. Eng. A* 498 (2008) 392–396.
- [35] C.C. Zhao, R.M. Niu, Y. Xin, D. Brown, D. McGuire, E.G. Wang, K. Han, *Mater. Sci. Eng. A* 799 (2021) 140091.
- [36] A. Gaganov, J. Freudenberger, E. Botcharova, L. Schultz, *Mater. Sci. Eng. A* 437 (2006) 313–322.
- [37] B.L. An, Y. Xin, R.M. Niu, J. Lu, E.G. Wang, K. Han, *Mater. Lett.* 252 (2019) 207–210.
- [38] P. Subramanian, D. Laughlin, D. Chakrabarti, *Bull. Alloy Ph. Diagr.* 9 (1988) 378–382.
- [39] D. Arias, J.P. Abriata, *J. Ph. Equilib.* 11 (1990) 452–459.
- [40] D.J. Chakrabarti, D.E. Laughlin, *J. Ph. Equilib.* 2 (1982) 455–460.
- [41] M.R. Baren, *Bull. Alloy Ph. Diagr.* 10 (1989) 640–640.
- [42] V. Raghavan, *J. Ph. Equilib. Diffus.* 31 (2010) 554–555.
- [43] K.A. Gschneidner, F.W. Calderwood, *Bull. Alloy Ph. Diagr.* 4 (1983) 375–377.
- [44] I. Karakaya, W.T. Thompson, *J. Ph. Equilib.* 13 (1992) 143–146.
- [45] R.P. Elliott, F.A. Shunk, W.C. Giessen, *Bull. Alloy Ph. Diagr.* 1 (1980) 41–45.
- [46] B.D. Cullity, S.R. Stock, in: *Elements of X-Ray Diffraction*, 3rd ed., Pearson India Education Services, Miejsce Nieznane, 2015, pp. 388–393.
- [47] H.W. King, *J. Mater. Sci.* 1 (1966) 79–90.
- [48] H.E. Kissinger, *Anal. Chem.* 29 (1957) 1702–1706.

- [49] W. Piyawit, W.Z. Xu, S.N. Mathaudhu, J. Freudenberger, J.M. Rigsbee, Y.T. Zhu, *Mater. Sci. Eng. A* 610 (2014) 85–90.
- [50] K. Han, A.A. Vasquez, Y. Xin, P.N. Kalu, *Acta Mater.* 51 (2003) 767–780.
- [51] C.C. Zhao, X.W. Zuo, E.G. Wang, K. Han, *Met. Mater. Int.* 23 (2017) 369–377.
- [52] X.W. Zuo, K. Han, C.C. Zhao, R.M. Niu, E.G. Wang, *J. Alloy. Compd.* 622 (2015) 69–72.
- [53] C.W. Corti, P. Cotterill, G.A. Fitzpatrick, *Int. Mater. Rev.* 19 (1974) 77–88.
- [54] C. Watanabe, R. Monzen, H. Nagayoshi, S. Onaka, *Philos. Mag. Lett.* 86 (2006) 65–73.
- [55] K. Han, A.C. Lawson, J.T. Wood, J.D. Embury, R.B. Von Dreele, J.W. Richardson, *Philos. Mag.* 84 (2004) 2579–2593.
- [56] K. Lücke, K. Detert, *Acta Metall.* 5 (1957) 628–637.
- [57] P.J. Clemm, J.C. Fisher, *Acta Metall.* 3 (1955) 70–73.
- [58] M. Bonvalet, X. Sauvage, D. Blavette, *Acta Mater.* 164 (2019) 454–463.
- [59] S. Divinski, M. Lohmann, C. Herzig, *Acta Mater.* 49 (2001) 249–261.
- [60] D. Raabe, M. Herbig, S. Sandlöbes, Y. Li, D. Tytko, M. Kuzmina, D. Ponge, P.P. Choi, *Curr. Opin. Solid State Mat. Sci.* 18 (2014) 253–261.
- [61] P. Lejcek, in: *Grain Boundary Segregation in Metals*, Springer, Berlin, Heidelberg, 2010, pp. 129–131.
- [62] J.D. Robson, *Acta Mater.* 61 (2013) 7781–7790.
- [63] B.C. Zhou, T. Yang, G. Zhou, H. Wang, J.H. Luan, Z.B. Jiao, *Acta Mater.* 205 (2020) 116561.
- [64] T. Gladman, *Mater. Sci. Technol.* 15 (1999) 30–36.
- [65] H. Mecking, in: K.H.J. Buschow, R.W. Cahn, M.C. Flemings, B. Ilshner, E.J. Kramer, S. Mahajan, P. Veysseyre (Eds.), *Encyclopedia of Materials: Science and Technology*, Elsevier, Oxford, 2001, pp. 9785–9794.
- [66] J.R. Davis, in: *Copper and Copper Alloys*, ASM International Handbook Committee, Materials Park, OH, 2001, p. 446.
- [67] E. Shizuya, T.J. Konno, in: Y. Fujikawa, K. Nakajima, T. Sakurai (Eds.), 2008 *Frontiers in Materials Research* 217–226.
- [68] Y.Z. Tian, S.D. Wu, Z.F. Zhang, R.B. Figueiredo, N. Gao, T.G. Langdon, *Acta Mater.* 59 (2011) 2783–2796.
- [69] Y.Z. Tian, S.D. Wu, Z.F. Zhang, R.B. Figueiredo, N. Gao, T.G. Langdon, *Mater. Sci. Eng. A* 528 (2011) 4331–4336.
- [70] J.D. Embury, R.M. Fisher, *Acta Metall.* 14 (1966) 147–159.
- [71] G. Frommeyer, G. Wassermann, *Acta Metall.* 23 (1975) 1353–1360.
- [72] P.M. Anderson, T. Foecke, P.M. Hazzledine, *MRS Bull.* 24 (1999) 27–33.
- [73] G. Dehm, B.N. Jaya, R. Raghavan, C. Kirchlechner, *Acta Mater.* 142 (2018) 248–282.
- [74] N. Li, J. Wang, A. Misra, J.Y. Huang, *Microsc. Microanal.* 18 (2012) 1155–1162.
- [75] A. Misra, J.P. Hirth, H. Kung, *Philos. Mag. A* 82 (2002) 2935–2951.
- [76] B. Shoykhet, M.A. Grinfeld, P.M. Hazzledine, *Acta Mater.* 46 (1998) 3761–3766.
- [77] S.O. Kasap, in: *Principles of Electronic Materials and Devices*, 4th ed., McGraw-Hill, New York, 2017, pp. 137–148.
- [78] C. Kittel, in: *Introduction to Solid State Physics*, 8th ed., Wiley, New York, 2005, pp. 139–151.
- [79] N.W. Ashcroft, N.D. Mermin, in: *Solid State Physics*, Saunders College, New York, 1976, pp. 5–9.
- [80] P.L. Rossiter, in: *The Electrical Resistivity of Metals and Alloys*, Cambridge University Press, Cambridge, 1987, pp. 190–223.
- [81] J.O. Linde, *Ann. Phys.* 407 (1932) 219–248.
- [82] E.J. Mittemeijer, in: *Fundamentals of Materials Science*, Springer, Berlin, Heidelberg, 2011, pp. 493–495.
- [83] L.M. Clarebrough, M.E. Hargreaves, M.H. Loretto, *Philos. Mag.* 7 (1962) 115–120.
- [84] J.G. Rider, C.T.B. Foxon, *Philos. Mag.* 16 (1967) 1133–1138.
- [85] J.D. Verhoeven, H.L. Downing, L.S. Chumbley, E.D. Gibson, *J. Appl. Phys.* 65 (1989) 1293–1301.
- [86] C.L. Trybus, W.A. Spitzig, *Acta Metall.* 37 (1989) 1971–1981.
- [87] F. Heringhaus, H.J. Schneider-Muntau, G. Gottstein, *Mater. Sci. Eng. A* 347 (2003) 9–20.
- [88] D. Mattissen, D. Raabe, F. Heringhaus, *Acta Mater.* 47 (1999) 1627–1634.
- [89] L. Qu, E.G. Wang, K. Han, X.W. Zuo, L. Zhang, P. Jia, J.C. He, *J. Appl. Phys.* 113 (2013) 173708.
- [90] E.H. Sondheimer, *Adv. Phys.* 1 (1952) 1–42.
- [91] J.R. Sambles, T.W. Preist, *J. Phys. F* 12 (1982) 1971–1987.
- [92] L. Tian, I. Anderson, T. Riedemann, A. Russell, *Acta Mater.* 77 (2014) 151–161.
- [93] D. Raabe, *Comput. Mater. Sci.* 3 (1995) 402–412.
- [94] J.B. Liu, L. Zhang, A.P. Dong, L.T. Wang, Y.W. Zeng, L. Meng, *Mater. Sci. Eng. A* 532 (2012) 331–338.
- [95] S.I. Hong, M.A. Hill, Y. Sakai, J.T. Wood, J.D. Embury, *Acta Metall.* 43 (1995) 3313–3323.
- [96] Y. Sakai, K. Inoue, T. Asano, H. Wada, H. Maeda, *Appl. Phys. Lett.* 59 (1991) 2965–2967.